Supporting Information For

π-Interactive Additive Unlocks Enhanced Zinc Anode Rechargeability: Unveiling Critical Role of Adsorption Layer Dynamics

Yuan Shang,[a] Yingna Ding, [a,#] Ravindra Kokate,[a,#] Ashutosh Rana,[c] Jeffrey E. Dick,[c,d] Xinyuan Wu,[e] Bram Hoex,[e] Mingyue, Wang,[f] Nana, Wang,[g] Qihui Zhang,[a] Priyank Kumar,[a,] Dipan Kundu[a,*]*

[a] *School of Chemical Engineering, UNSW Sydney, Kensington, NSW 2052, Australia*

[c] *Department of Chemistry, Purdue University, West Lafayette, IN, 47907, USA*

[d] *Elmore Family School of Electrical and Computer Engineering, Purdue University, West Lafayette, IN, 47907, USA*

[e] *School of Photovoltaic and Renewable Energy Engineering, UNSW Sydney, Kensington, NSW 2052, Australia*

[f] *Institute for Superconducting and Electronic Materials, Faculty of Engineering and Information Sciences, University of Wollongong, North Wollongong, NSW 2500, Australia*

[g] *Centre for Clean Energy Technology, School of Mathematical and Physical Sciences, Faculty of Science, University of Technology Sydney, Sydney, NSW, 2007 Australia*

#Equal contributions

*Corresponding author.

Priyank Kumar; Email: priyank.kumar@unsw.edu.au

Dipan Kundu; Email: d.kundu@unsw.edu.au

Experimental Methods

Material. Cyclohexanol, phenol, 4-chlorophenol, 3-nitrophenol and 4-nitrophenol were purchased from Sigma-Aldrich without further treatment. The $ZnSO_4{\cdot}7H_2O$ (99.5%), $Zn(CH_3CO_2)_2$ (99.99%) and V_2O_5 (99%) were also obtained from Sigma Aldrich.

Preparation of the Electrolytes. $ZnSO_4{\cdot}7H_2O$ was dissolved in Milli-Q water to prepare 1M $ZnSO_4$ baseline. Similarly, different concentrations of additives (cycloaliphatic or aromatic molecules) and $ZnSO_4{\cdot}7H_2O$ were mixed in Milli-Q water to prepare an additive-containing 1M $ZnSO_4$ electrolyte.

Preparation of $Zn_{0.25}V_2O_5 \cdot nH_2O$ Cathode Material. First, 20 mg of reduced graphene oxide (rGO) was ultrasonically dispersed in 50 mL of a water/acetone mixture (15:1 volume ratio). Next, 2 mmol of V_2O_5 and 1.3 mmol of $Zn(CH_3CO_2)_2$ were directly introduced into the dispersion and keep vigorous stirring for 1 h. The resulting solution was then transferred into a 100 mL Teflon-lined stainless-steel autoclave (Parr Instrument) and maintained at 180°C for 48 hours. Finally, the obtained product was collected via filtration and washed three times with water and ethanol.

Electrochemical Measurement. Zinc foil (⩾99.9%) with varying thicknesses of 100, 30, and 20 μm was punched into 1 cm^2 disc (geometric surface area) for both half-cell and full-cell investigations. Zinc plating and stripping experiments were conducted in a Swagelok-type cell, utilizing either a Ti/Zn asymmetric or Zn/Zn symmetric configuration. A binder-free glass fiber filter (APFF12450, Merck Millipore Ltd.) was employed as the separator, with 50 μL of electrolyte. Prior to use, Ti and Zn electrodes were polished using an alumina powder slurry and sequentially washed with water and ethanol. Cell assembly and all related handling were carried out under ambient conditions. The galvanostatic cycling studies were done on the LAND CT3002AU cycler. The EIS (VMP-3, BioLogic) was performed in a three-electrode (Zn||Zn||Zn) configuration, ranging from the 1 MHz to 0.1 Hz frequency range with AC amplitude of 10 mV, to probe the charge transfer kinetics of Zn deposition. The obtained EIS data are deconvoluted by the Python-based pyDRTtools software developed by Ciucci's lab. The second-order Gaussian radial basis functions (RBF) with shape factor control between 0.75 to 1.0 and a regularization parameter of 0.001 was selected for DRT analysis.[17–19]

The ionic conductivity was obtained in a symmetric (Ti||Ti) configuration by EIS, derived from the intercept of the Nyquist plot on the real (impedance, Z) axis, and the ionic conductivity was calculated according to the following equation:

$$\sigma = \frac{L}{R_s A}$$

where σ (S cm^{-1}) stands for the ionic conductivity, R_s is the electrolyte resistance obtained from EIS, L (cm) is the distance between the two Ti electrodes, and A is the Ti electrode area (cm^{-2}). LSV measurements were conducted in a three-electrode setup using 1 M Na_2SO_4 as the electrolyte, adjusted to match the pH of 1 M $ZnSO_4$ (same for other testing involving this replacement), to prevent current interference from Zn deposition during the cathodic sweep. The scan rate was set to 1 mV s^{-1}, with Ti serving as the working electrode, Pt as the counter electrode, and Ag/AgCl as the reference. For Tafel analysis, potentiodynamic polarization was performed under similar conditions, except with Zn as the working electrode. Additionally, cyclic voltammetry (CV) was carried out in a Zn||Zn symmetric cell at a scan rate of 1 mV s^{-1} to examine Zn plating and stripping behavior.

CV at high scan rates of 60 V s^{-1} was performed to evaluate the kinetics and coulombic efficiency (CE) of zinc deposition. The measurements were carried out in a two-electrode configuration, employing a tungsten ultramicroelectrode as the working electrode and an Ag/AgCl electrode as the reference/counter electrode.

The Zn electrode was precisely weighed before being assembled into the Zn||Ti cell to quantify the initial capacity. The asymmetric cell then underwent galvanostatic charge/discharge cycling for 10, 30, and 50 cycles, as presented in **Figure S27**. After that, the Zn electrode was fully stripped using the same current to determine the remaining Zn capacity, allowing for an accurate assessment of capacity loss over cycling.

To investigate the adsorption behavior of organic additives on the electrode surface, 4-chlorophenol, phenol, and cyclohexanol were selected as model compounds representing strong, moderate, and weak adsorptive additives, respectively. A series of aqueous solutions was prepared by dissolving each additive in 1 M Na_2SO_4 at concentrations ranging from 0.001

M to 0.3 M. Linear sweep voltammetry (LSV) was carried out in each solution using a three-electrode system comprising a zinc working electrode, a Pt electrode, and an Ag/AgCl reference electrode. The surface coverage (θ) of each additive was calculated by comparing the corrosion current (obtained by Tafel fitting) in the presence of the additive with that in the blank 1M Na_2SO_4 solution, using Equation 4. This surface coverage was then plotted as a function of additive concentration to derive the corresponding adsorption isotherms.
The ZVO cathode was prepared by mixture with conductive carbon (Super P, Timcal) and a styrene-butadiene rubber/sodium carboxymethyl cellulose (SBR/CMC) binder (weight ratio of 70:25:5) in deionized water. The mixture underwent ultrasonic treatment for 3 hours, followed by vacuum filtration to produce free-standing electrode discs. These electrodes were then vacuum-dried at 80°C for overnight. Finally, 1 cm^2 electrode discs, with an average ZVO active material loading of approximately 3–11 mg cm^{-2}, were punched out for various full-cell studies, as shown in **Figure 5**.

Physicochemical Characterization. X-ray diffraction (XRD) analysis was performed using a PANalytical Xpert Multipurpose X-ray Diffraction System (MPD) with Cu Kα radiation to detect the corrosion byproducts in various electrolytes. XRD patterns were collected over a 2θ range of 5° to 80° at a scanning speed of 0.04° s^{-1}. The three-dimensional surface morphology of cycled Zn electrodes was analyzed using a laser scanning confocal microscope (LSCM, VK-X250, Keyence Co., Osaka, Japan), which enables non-contact profiling and roughness measurements with nanometer resolution. The microstructural characteristics of both cycled (during early deposition and long-term cycling) and rested Zn electrodes (after 24 h immersed in the electrolyte) were further investigated using a FEI Nova NanoSEM 230 field emission scanning electron microscope. Additionally, Raman spectroscopy was obtained from a Renishaw inVia Raman spectrometer under a 532 nm argon ion laser (power 5%), to probe the solvation structure of Zn^{2+}.

QCM-D measurements were conducted using the Q-sense Explorer system (Biolin Scientific AB) at 25 °C. The fundamental frequency, along with five harmonics (1:3, 1:5, 1:7, 1:9 and 1:11), was recorded simultaneously, accompanied by the corresponding dissipation factors. The gold-coated AT-cut quartz crystal sensor (fundamental frequency ≈4.95 MHz) was sourced from Q-sense (QX301). Prior to testing, the sensor underwent a 10-minute UV/ozone treatment, followed by immersion in a cleaning solution composed of a 5:1:1 mixture of Milli-Q water, ammonia (25%), and hydrogen peroxide (30%) at 75 °C for 5 minutes. It was then thoroughly rinsed with Milli-Q water, dried with nitrogen gas, and subjected to an additional 10-minute UV/ozone treatment. To establish a stable baseline for frequency and dissipation, a 1 M $ZnSO_4$ buffer solution was introduced at the start of the measurement. Subsequently, the electrolyte-containing additives was introduced into the sensor at a controlled flow rate of 0.1 mL min^{-1}. The acquired QCM-D data were analyzed using the "Broadfit" viscoelastic model in the Q-tools software (Q-sense). Upon introduction of additive-containing electrolytes, distinct frequency (Δf) and dissipation (Δdissipation) shifts occur, indicating the adsorption of organic molecules onto the surface. The magnitude and nature of these shifts suggest the formation of soft, viscoelastic films with varying degrees of rigidity depending on the additive. Notably, the reversibility of adsorption is confirmed by the return of both frequency and dissipation signals to baseline upon rinsing with additive-free electrolyte.

Theoretical Computation. For all the adsorption energy calculations, we utilized the same computational methodology as described in our previous work,[4] employing the Vienna Ab-initio Simulation Package (VASP).[20,21] Adjustments were made to ensure accurate adsorption energy calculations, including optimizing the vacuum spacing and correcting the BPARAM value to 11.95. The Zn {100}hexagonal surface slab, consisting of 144 Zn atoms, was modeled with a vacuum layer of ~10 Å thickness to prevent periodic interactions. Molecular structures

were sourced from the PUBChem[22] and initially relaxed using the same parameters and computational methods to obtain optimized geometries. Adsorption energies for the newly introduced additives were computed for two distinct configurations: "head" interactions, where only the hydroxyl (OH) group interacts with the zinc surface, and "flat" interactions, where the entire molecular structure interacts with the zinc surface. These calculations employed the rVV10 nonlocal correlation functional combined with the r2SCAN meta-GGA, ensuring improved numerical efficiency and accuracy. All calculations adhered to convergence criteria of $1 \times 10{-}5\ eV$ for electronic wavefunctions and $5 \times 10{-}2\ eV$ Å−1 for maximal force components, ensuring consistent and reliable results.

For solvation energy calculations, we adopted a two-step computational approach to enhance precision. Following the methodology from our previous study,[4] we first optimized the molecular geometries using DFT calculations in VASP to locate the global energy minima, employing the same parameters used in the adsorption energy calculations. The resulting optimized structures were then used as inputs for gas-phase solvation energy calculations, and the gas-phase optimized geometries were subsequently used as initial inputs for aqueous-phase solvation energy calculations performed using Gaussian16.[23] This modification, compared to directly using guess structures in previous solvation energy calculations, resulted in a noticeable improvement in accuracy and consistency. Consequently, this refined strategy was applied to both previously studied additives and newly introduced phenol-based and acidic molecules, ensuring methodological consistency across all calculations.

For pKa values, most of the data were sourced from ChemicalBook, ensuring consistency with the datasets to maintain comparability and reliability in correlating pKa with additive performance. To investigate how the pKa of the molecules affects hydrogen dissociation (OH bond length change) from their hydroxyl (OH) groups, we performed gas-phase and water-phase calculations using Gaussian16. All molecules were initially optimized in the gas phase at the M062X/6-31+G(d) level of theory. Subsequently, water-phase optimizations were performed using the gas-phase optimized structures as inputs, employing the same level of theory with the additional keyword SCRF=(SMD, Solvent=Water) to apply the SMD implicit solvent model. Vibrational analysis confirmed that the optimized geometries had zero imaginary frequencies, verifying them as true minimum-energy structures. To further capture explicit interactions with water molecules, a hybrid water model was constructed by surrounding each molecule with 10 explicit H_2O molecules in the aqueous medium. The OH bond lengths were calculated for the gas-phase optimized structures and for the structures after water-phase optimization, and the OH bond length change percentage was subsequently determined. For molecules containing more than one OH group, the largest observed OH bond length change was considered for further analysis

Table S1. pKa values, calculated adsorption energies (for both flat and head interactions), and solvation energies of various additives.

Additive	pKa	Adsorption (eV) (head)	Adsorption (eV) (flat)	Solvation (kcal/mol)
phenol	9.98	-0.69	-0.88	-6.92
4-chlorophenol	9.24	-0.51	-0.94	-7.21
4-nitrophenol	7.15	-0.52	-1.24	-9.41
3-nitrophenol	8.36	-0.56	-1.35	-8.82
cyclohexanol	16	-0.89	-0.83	-5.7

Table S2. Changes in OH bond lengths of the additives after hybrid water model calculations, along with their corresponding pKa values.

Additives	pKa	OH, bond length change (%)
propanol	16.85	1.43
hexanol	16.84	1.61
butanol	16.1	1.89
cyclohexanol	16	2.37
ethanol	15.9	1.46
pentanol	15.24	2.18
1-3-butanediol	14.83	2.14
1-4-butanediol	14.73	2.51
2-3-butanediol	14.67	2.00
1-2-heptanediol	14.6	2.21
1-2-octanediol	14.6	2.26
1-2-butanediol	14.49	2.08
1-2-hexanediol	14.49	2.44
1-2-ethanediol	13.61	2.04
1-2-pentanediol	14.49	2.34
1-2-propanediol	14.49	2.25
phenol	9.98	2.94
4-chlorophenol	9.24	3.21
3-nitrophenol	8.36	2.87
4-nitrophenol	7.15	3.94

Table S3. Adsorption energies of the additives before and after hydrogen dissociation, and hydrogen dissociation percentages determined from pH change measurements.

Additives	pKa	Adsorption (eV) (before dissociation)	Adsorption (eV) (after dissociation)
cyclohexanol	16	-0.83	/
phenol	9.98	-0.88	-2.82
4-chlorophenol	9.24	-0.94	-2.38
3-nitrophenol	8.36	-1.35	-2.92
4-nitrophenol	7.15	-1.24	-2.5

Table S4. Parameters of cyclohexanol-containing electrolytes for adsorption isotherm fitting.

Cyclohexanol Concentration (C, mol L^{-1})	I_{corr} (μA cm^{-2} from Tafel)	Surface Coverage (θ)	lnθ	lnC	ln(θ/(1-θ))	ln(θ/c*(1-θ))
0.3	3.2	0.90	-0.10	-1.20	2.23	3.69
0.2	3.5	0.89	-0.11	-1.61	2.11	4.57
0.1	3.1	0.91	-0.1	-2.30	2.26	4.97
0.05	4	0.88	-0.13	-3.00	1.98	5.52
0.025	4.6	0.86	-0.15	-3.69	1.83	5.81
0.02	4.3	0.87	-0.14	-3.91	1.90	6.21
0.015	3.9	0.88	-0.13	-4.20	2.01	6.84
0.005	4.1	0.88	-0.13	-5.30	1.95	7.24
0.001	4.0	0.88	-0.13	-6.91	1.99	8.89
0	32.9	/	/	/	/	/

Table S5. Parameters of phenol-containing electrolytes for adsorption isotherm fitting.

Phenol Concentration (C, mol L^{-1})	I_{corr} (μA cm^{-2} from Tafel)	Surface Coverage (θ)	lnθ	lnC	ln(θ/(1-θ))	ln(θ/c*(1-θ))
0.3	4.8	0.85	-0.16	-1.20	1.77	2.97
0.2	5.6	0.83	-0.19	-1.61	1.59	3.20
0.15	7.3	0.78	-0.25	-1.90	1.25	3.15
0.1	12.6	0.62	-0.48	-2.30	0.48	2.78
0.05	19.3	0.41	-0.88	-3.00	-0.35	2.65
0.025	20.5	0.38	-0.97	-3.69	-0.50	3.19
0.02	23.0	0.30	-1.20	-3.91	-0.84	3.07
0.015	24.9	0.24	-1.41	-4.20	-1.13	3.07
0.01	29.8	0.09	-2.36	-4.61	-2.27	2.34
0	32.9	/	/	/	/	/

Table S6. Parameters of 4-chlorophenol-containing electrolytes for adsorption isotherm fitting.

4-chlorophenol Concentration (C, mol L^{-1})	I_{corr} (μA cm^{-2} from Tafel)	Surface Coverage (θ)	lnθ	lnC	ln(θ/(1-θ))	ln(θ/c*(1-θ))
0.2	5.4	0.84	-0.16	-1.61	1.62	3.23
0.15	6.5	0.80	-0.19	-1.90	1.40	3.30
0.1	2.9	0.91	-0.25	-2.30	2.32	4.62
0.05	2.7	0.92	-0.48	-3.00	2.40	5.39
0.025	4.2	0.87	-0.88	-3.69	1.93	5.62
0.02	3.6	0.89	-0.97	-3.91	2.11	6.03
0.015	18.6	0.44	-1.20	-4.20	-0.26	3.94
0.01	25.8	0.22	-1.41	-4.61	-1.29	3.31
0.005	29.2	0.11	-2.36	-5.30	-2.05	3.25
0	32.9	/	/	/	/	/

Details on Additive Adsorption Isotherm Analysis

The dynamic adsorption of the additive on the zinc metal surface can be expressed by the following reversible reaction[6]:

$$Ad(aq) + xH_2O(ads) \rightleftarrows Ad(ads) + xH_2O(aq) \quad (1)$$

where Ad and H_2O refer to the additive and water, and ads and aq in parentheses represent additive/H_2O in the adsorbed state (on metal) and in the solution phase, respectively. Assuming that each additive molecule replaces only one adsorbed water molecule and that the concentration of water in the solution remains constant, the adsorption constant (K_{ads}) associated with Reaction (1) at equilibrium can be expressed by Equation (2).[7]

$$K_{ads} = \frac{C_{ad(ads)}}{C_{ad(aq)} \cdot C_{H_2O(ads)}} \quad (2)$$

Where $C_{ad(ads)}$ and $C_{ad(aq)}$ represent the concentration of the additive in the adsorption layer and solution, respectively, and $C_{H_2O(ads)}$ is the concentration of water in the adsorbed layer. Furthermore, $C_{ad(ads)}/C_{H_2O(ads)}$ is dimensionless and is equivalent to the extent of surface coverage (θ) of the additive, which can be obtained from the zinc corrosion inhibition owing to additive adsorption. Therefore, (2) can be rewritten as (3).

$$K_{ads} \cdot C_{ad(aq)} = \theta \quad (3)$$

$$where\ \theta = 1 - \frac{I_{corr}}{I_{corr}^0} \quad (4)$$

Where the I_{corr}, and I_{corr}^0 corresponds to the corrosion current with and without additives, respectively. The corrosion current is obtained by Tafel analysis with the Na_2SO_4 electrolyte, where the adsorption of the additive on the metal surface suppresses the HER current relative to the additive-free electrolyte. Accordingly, cyclohexanol, phenol, and 4-chlorophenol were selected as representative additives with concentrations from 0 mM to 300 m M in 1M Na_2SO_4 solution (**Table S4-6**) to probe additive–metal surface interactions, given their distinct physicochemical properties, including pKa, molecular structure, and adsorption energy. The θ and the additive concentration relationship were then analyzed based on the different adsorption isotherm models (see supporting information) to extract parameters relevant to the additive–zinc metal interaction and additive organization at the zinc-electrolyte interface.

Freundlich adsorption isotherm

Given the adsorption process of the additive on the metal surface, it involves the displacement of adsorbed water molecules at the interface by additive molecules, which is not necessarily a one-to-one fashion. Besides, the inherent surface defects and protrusions on the zinc metal indicate the heterogeneous nature of the electrode surface. In this regard, the most common adsorption isotherm- Langmuir isotherm,[1] is not applicable due to its assumption of a homogeneous surface. Instead, the Freundlich adsorption isotherm (Equation (1)) is employed here, incorporating a coefficient n to characterize the deviation from the linearity of the Langmuir model, arising from the surface heterogeneity and non-equivalent adsorption site replacement.[2]

$$K_{ads} \cdot C_{adv(aq)}^{1/n} = \theta \quad (1)$$

$$lnK_{ads} + \frac{1}{n} ln\, C_{adv(aq)} = ln\theta \quad (2)$$

Here, Equation (2) represents the logarithmic form of Equation (1), which describes a linear relationship between $ln\, C_{adv(aq)}$ and $ln\theta$.

Frumkin adsorption isotherm

The Frumkin adsorption isotherm introduces an interaction factor α_F to investigate where the interaction between molecules adsorbed at the metal-solution interface occurs.[3] Hence, the adsorption model can be expressed by Equation (3).

$$K_{ads} \cdot C_{adv} = \frac{\theta}{1-\theta} \exp(-2\alpha_F \times \theta) \quad (3)$$

Where α_F (as Frumkin's constant can reveal the force of the interaction between the adsorbed additive. It is nevertheless a statistical factor evaluated under Equation (4)

$$\alpha_F = \frac{n_a \varphi}{2kT} \quad (4)$$

where n_a denotes the number of organic additive molecules interacting with a single adsorbed molecule, φ – the energy of interaction between a pair of molecules, and k- Boltzmann's constant. The intermolecular interactions among inhibitor species are generally weak and primarily governed by dipole–dipole forces.[4]

By expressing Equation (4) in logarithmic form, its linearized version can be obtained, as shown in Equation (5):

$$ln\, \frac{\theta}{C_{adv}(1-\theta)} = lnK_{ads} + 2\alpha_F\theta \quad (5)$$

The linearized form of the Frumkin isotherm establishes a relationship between the $\frac{\theta}{C_{adv}(1-\theta)}$ term and the surface coverage θ. From the slope of the resulting linear plot, the interaction parameter a_F can be obtained. The interaction parameter plays a critical role in distinguishing whether additive molecules preferentially adsorb onto the metal surface or tend to form intermolecular self-associated layers.[2] When $a_F = 0$, the Frumkin isotherm reduces to the classical Langmuir isotherm. A negative value reflects repulsive interactions between adsorbed molecules, whereas a positive value indicates attractive forces. According to Equation

(5), a negative slope corresponds to a larger intercept, indicating a greater magnitude of the Gibbs free energy of adsorption and thus stronger metal–inhibitor interactions. This arises because intermolecular repulsion allows inhibitor molecules to adopt more favorable orientations for surface binding. Conversely, when $a_F > 0$, the interactive intermolecular force restricts the configurational freedom of the adsorbed species, limiting their ability to optimize interactions with the metal surface and thus weakening the overall adsorption strength.

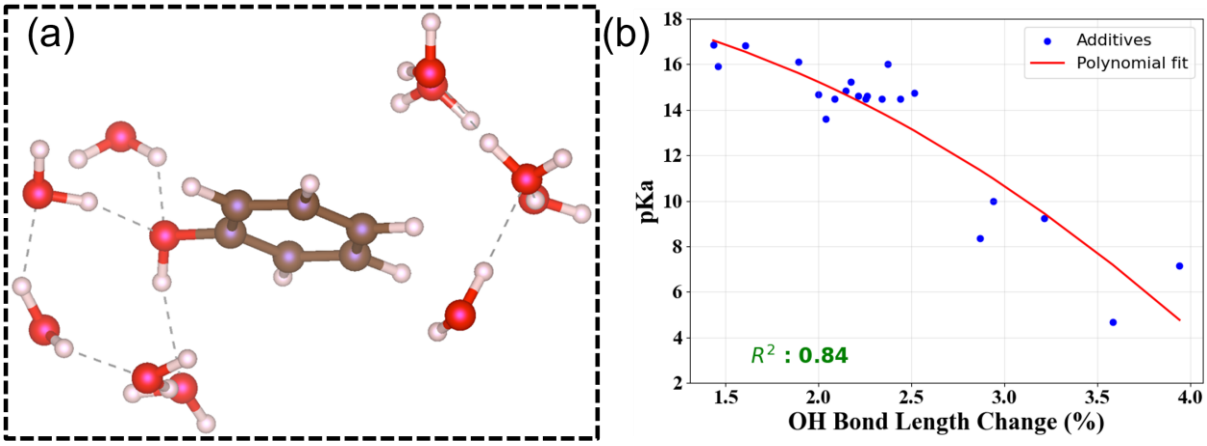

Figure S1. (a) Hybrid water model structure used for calculating OH bond length change in the phenol molecule. (b) Correlation between the pKa values of the additives and the percentage change in their OH bond lengths.

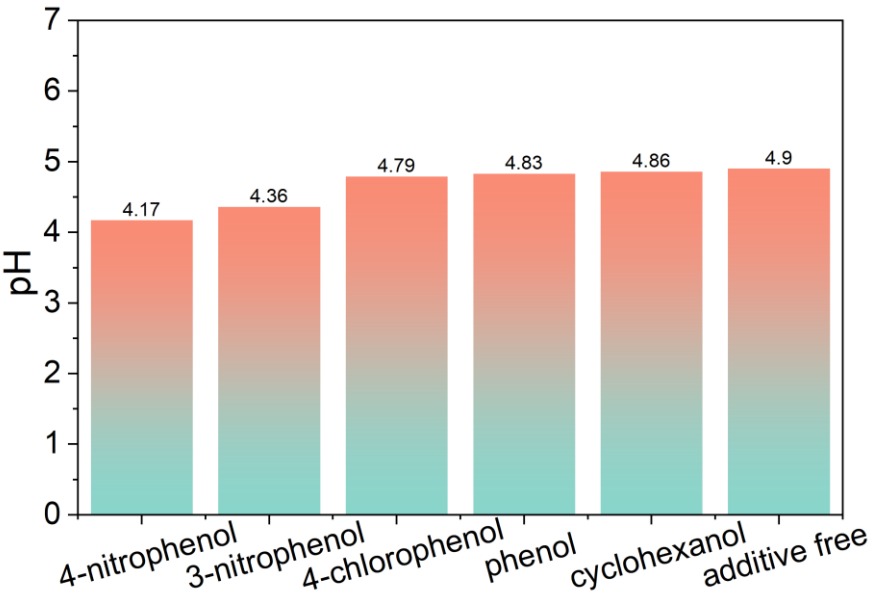

Figure S2. The pH of 1M $ZnSO_4$ baseline electrolyte and the pH after dissolving 50 mM additive in this baseline solution.

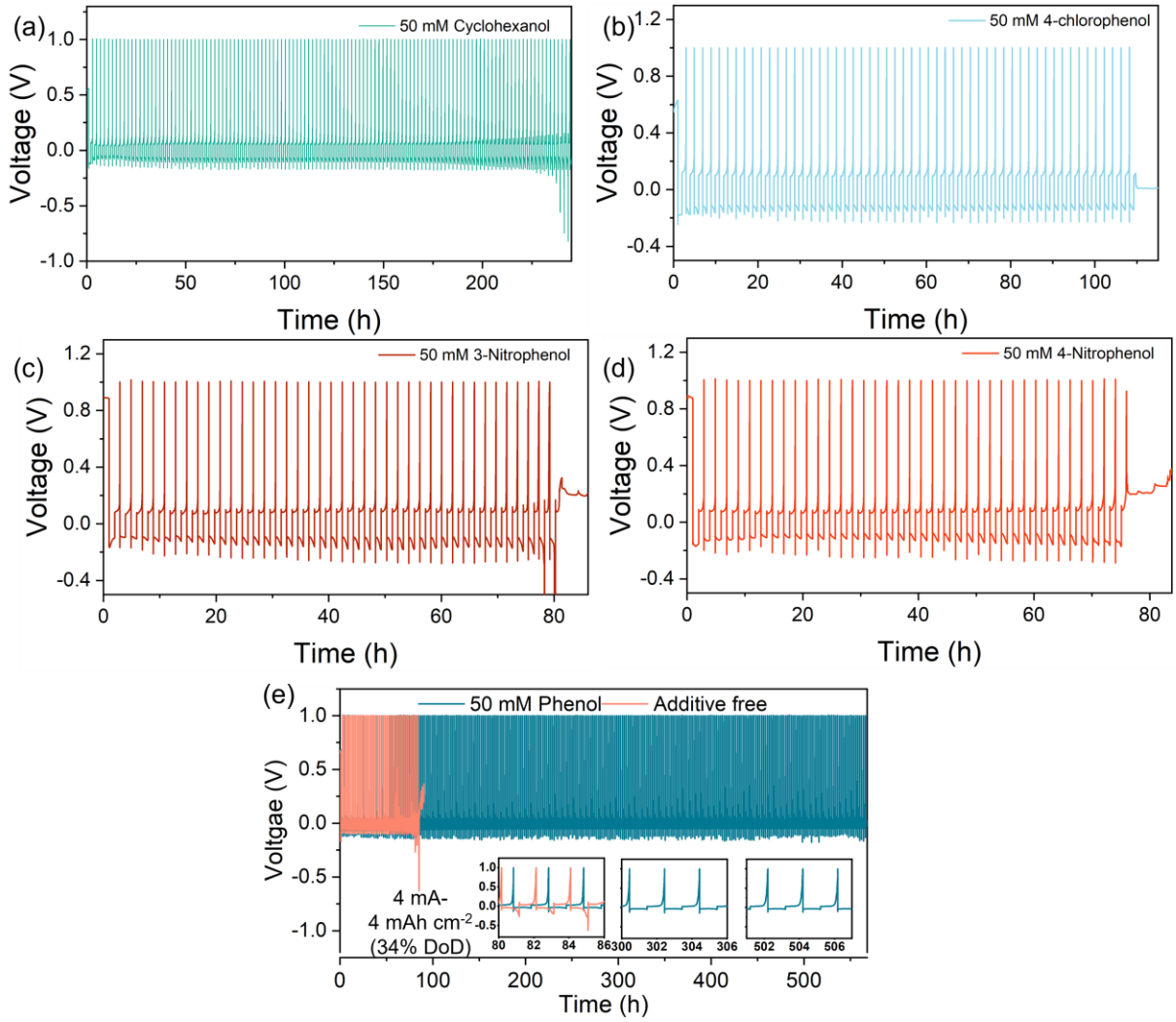

Figure S3. The galvanostatic zinc cycling in Zn||Ti configuration with (a) 50 mM cyclohexanol, (b) 50 mM 4-chlorophenol, (c) 50 mM 3-nitrophenol, (d) 50 mM 4-nitrophenol, (e) and 50 mM phenol in the 1M $ZnSO_4$ electrolyte along with baseline electrolyte at 4 mA cm^{-2} and 4 mAh cm^{-2}.

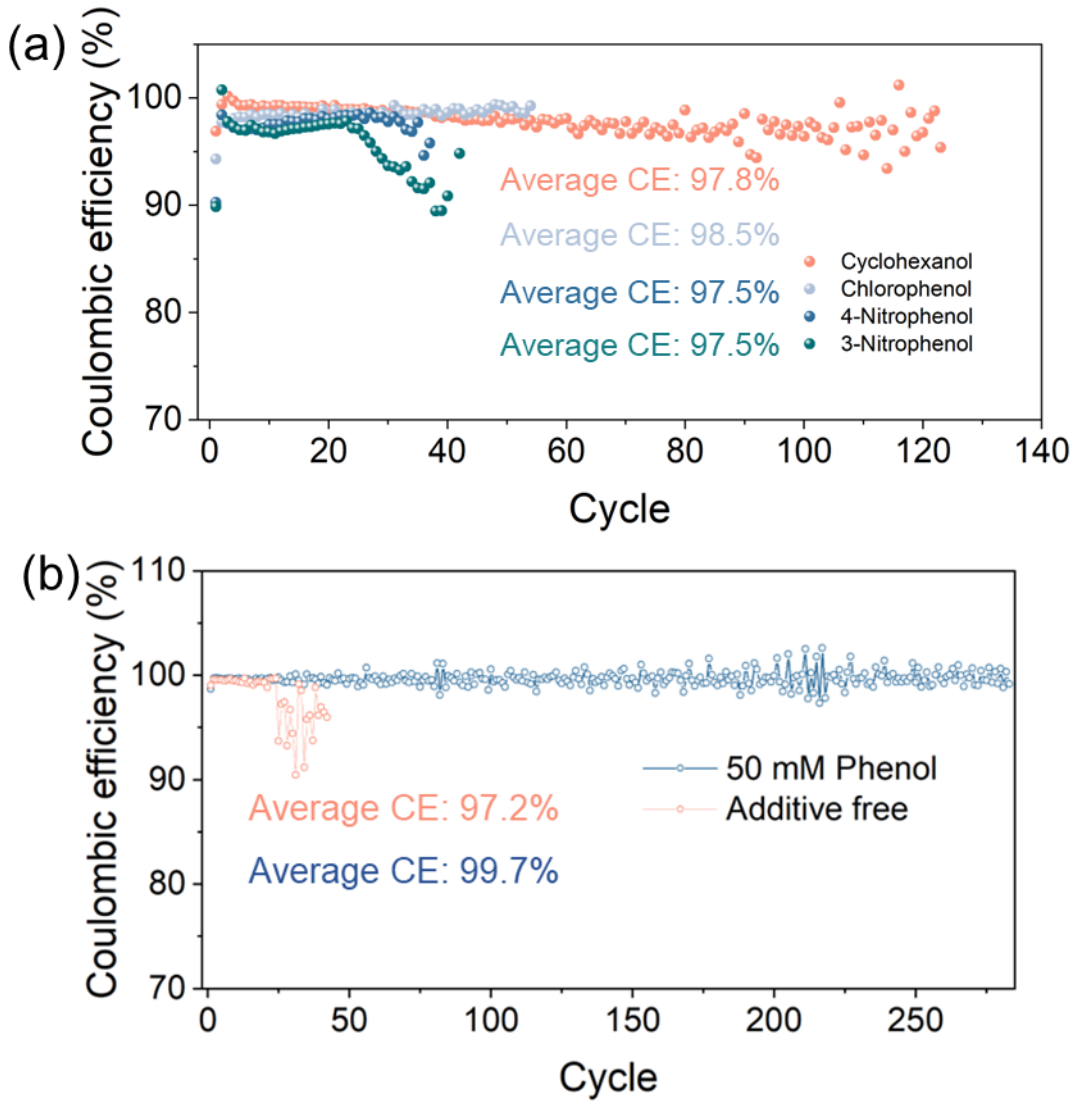

Figure S4. The corresponding Coulombic efficiency for the cells cycled at 4 mA cm^{-2}-4 mAh cm^{-2} in (a) 50 mM phenol and 1M $ZnSO_4$ electrolyte and (b) other additive-containing electrolytes.

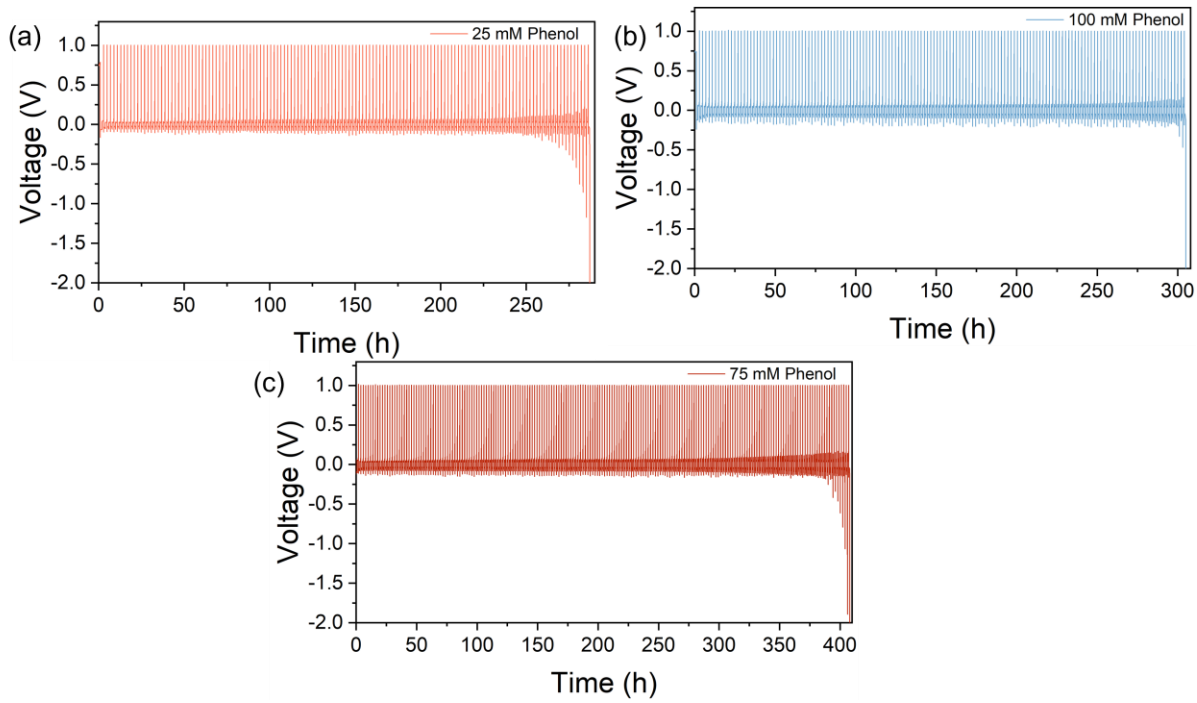

Figure S5. The galvanostatic zinc cycling in Zn||Ti configuration with (a) 25 mM, (b) 50 mM, (c) 75 mM phenol electrolyte at 4 mA cm^{-2} and 4 mAh cm^{-2}.

QCM-D Measurement

QCM-D measurements were conducted to monitor additive adsorption at the metal-electrolyte interface. The experiment followed a three-step protocol: (1) flowing 1 M $ZnSO_4$ over the sensor and baseline establishment by normalizing the frequency and dissipation shift caused by salt/water adsorption, (2) introduction of additive-containing electrolyte to observe adsorption-induced shifts, and (3) reintroduction of baseline electrolyte to assess reversibility. The quartz crystal's resonant frequency (Δf) decreases with mass accumulation due to adsorption, while energy dissipation (ΔD) reflects the viscoelastic nature of the adsorbed layer. During the second step, introduction of the additive-containing electrolytes induces varying degrees of frequency shift, hinting that the organic additives adsorb on the quartz crystal surface to different extents. High dissipation values (ΔD > 1 ppm) and nonlinear Δf–ΔD trends across harmonics suggest the formation of soft, dynamic films. Upon rinsing, both Δf and ΔD return to baseline, confirming reversible adsorption behavior for all tested additives (Figures S6–S10).

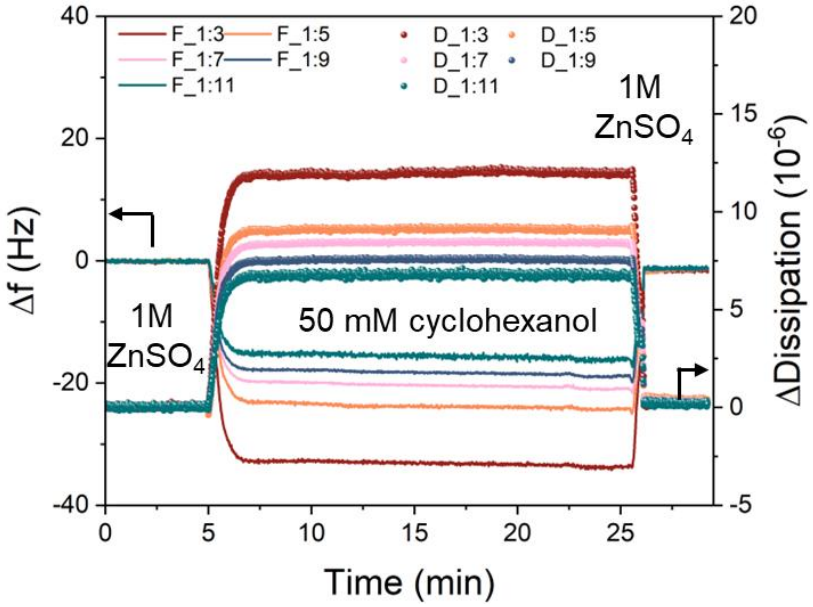

Figure S6. QCM-D measurement to visualize the cyclohexanol additive filming at the metal surface. F_1:X (X=3, 5, 7, 9, 11) represent different harmonics, and D_1:X (X = 1, 3, 5, 9, 11) represent different dissipation values

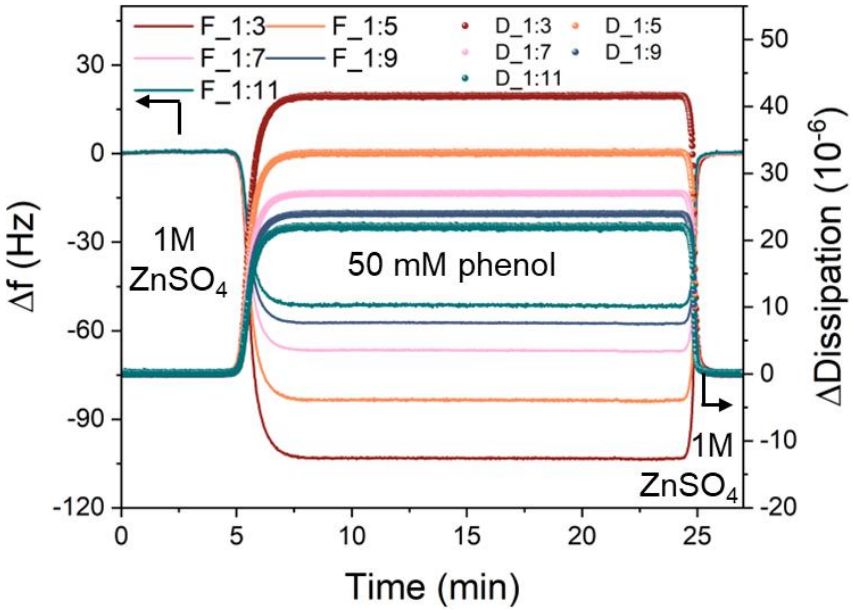

Figure S7. QCM-D measurement to visualize the phenol additive filming at the metal surface.

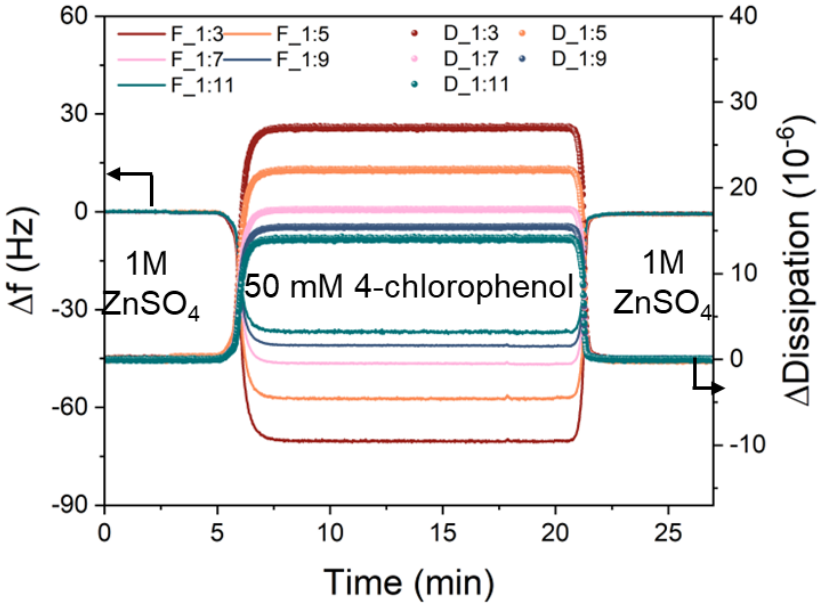

Figure S8. QCM-D measurement to visualize the 4-chlorophenol additive filming at the metal surface.

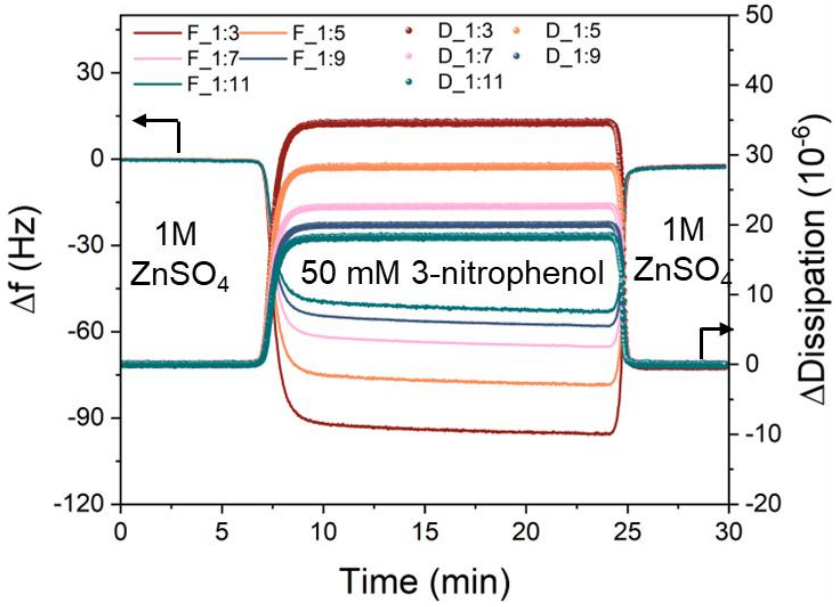

Figure S9. QCM-D measurement to visualize the 3-nitrophenol additive filming at the metal surface.

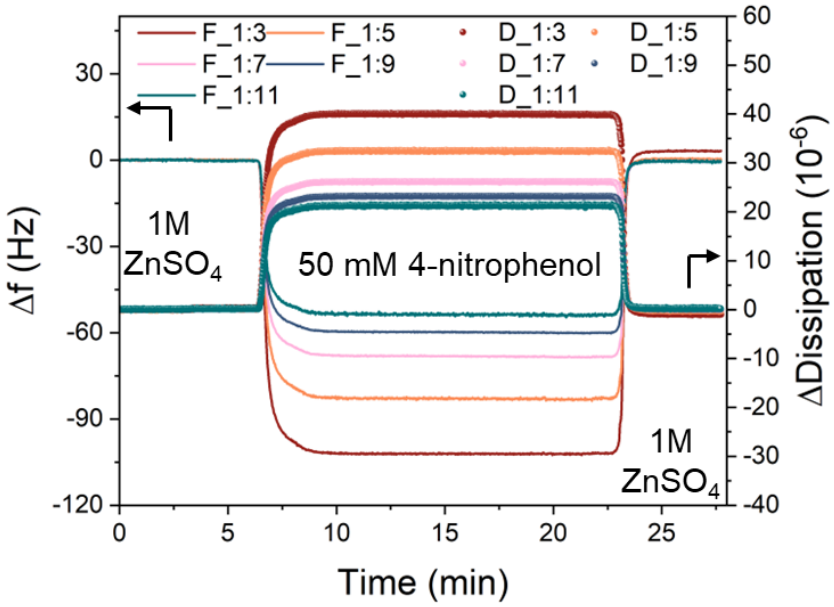

Figure S10. QCM-D measurement to visualize the 4-nitrophenol additive filming at the metal surface.

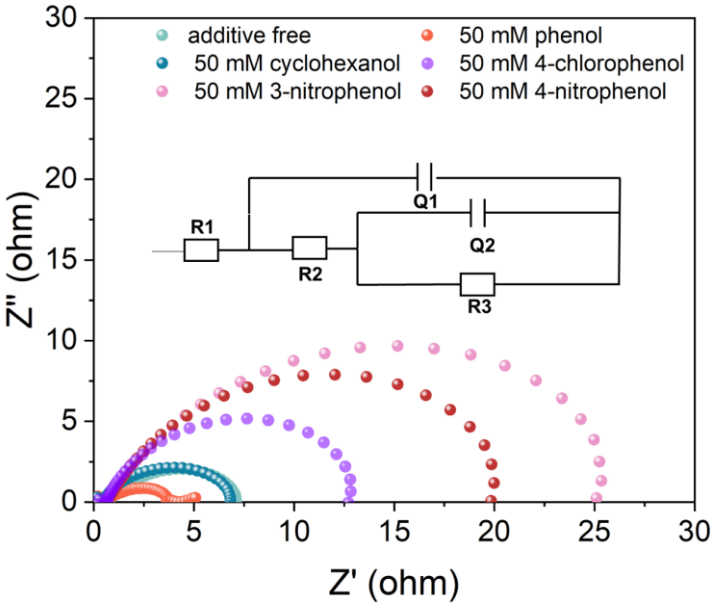

Figure S11. The Nyquist plot obtained from the Zn-Zn-Zn three-electrode configuration after 5 cycles in different electrolytes.

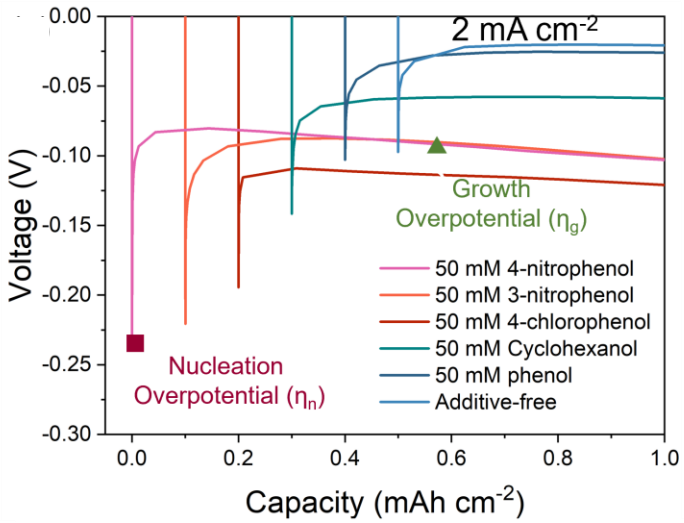

Figure S12. Galvanostatic voltage profile for different electrolytes to demonstrate different overpotential regimes, measured after 5 cycles at current of 2 mA cm^{-2}.

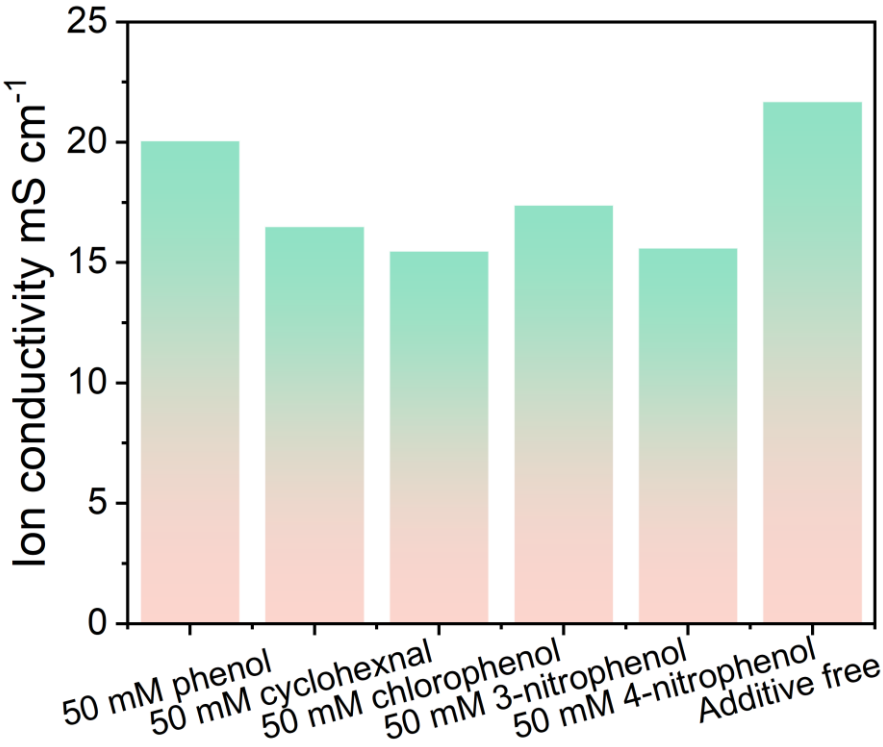

Figure S13. Ionic conductivity of different additive-containing electrolytes.

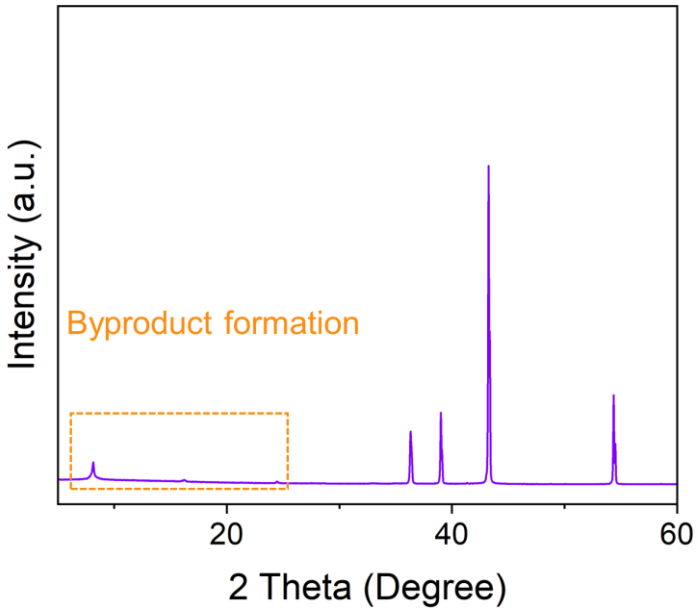

Figure S14. XRD pattern of Zn electrode after 10 cycles in 50 mM 4-chlorophenol electrolyte.

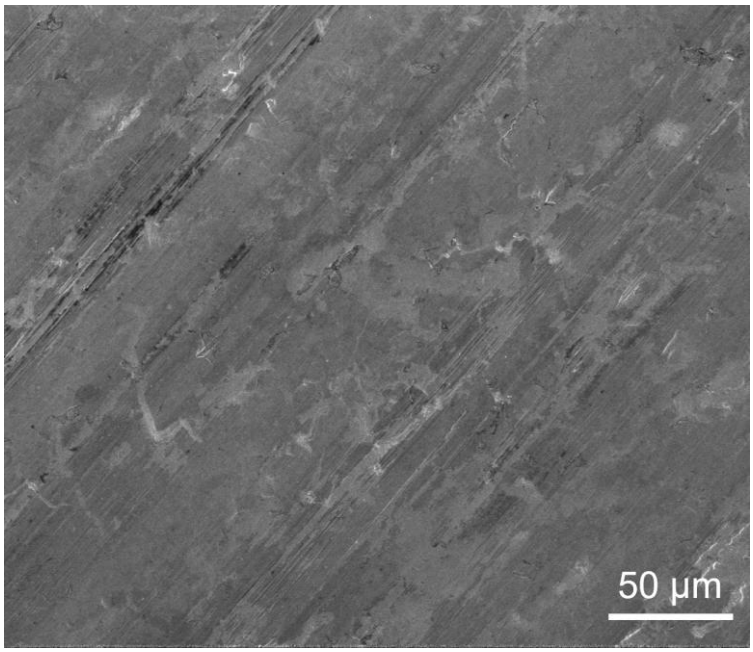

Figure S15. SEM image of pristine Zn foil.

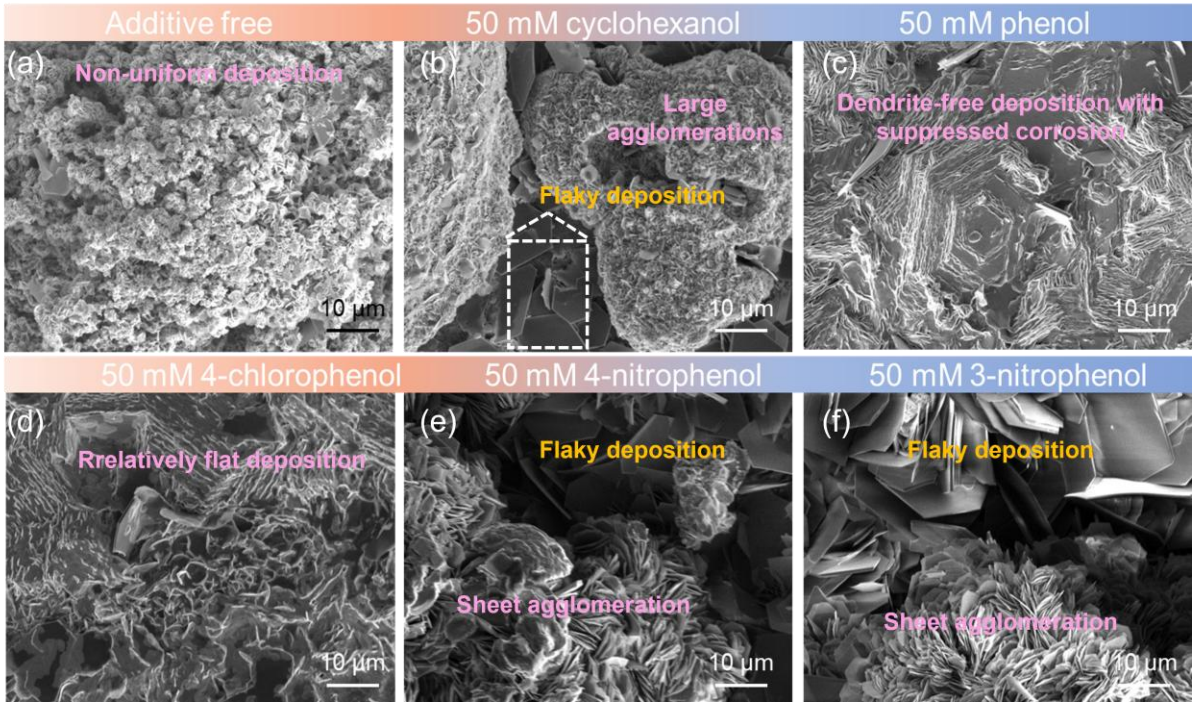

Figure S16. The Zn electrode morphology after 10th plating in (a) additive-free, (b) 50 mM cyclohexanol, (c) 50 mM phenol, (d) 50 mM 4-chlorophenol, (e) 50 mM 4-nitrophenol, and (f) 50 mM 3-nitrophenol electrolytes under 2 mA cm^{-2} and 2 mAh cm^{-2}

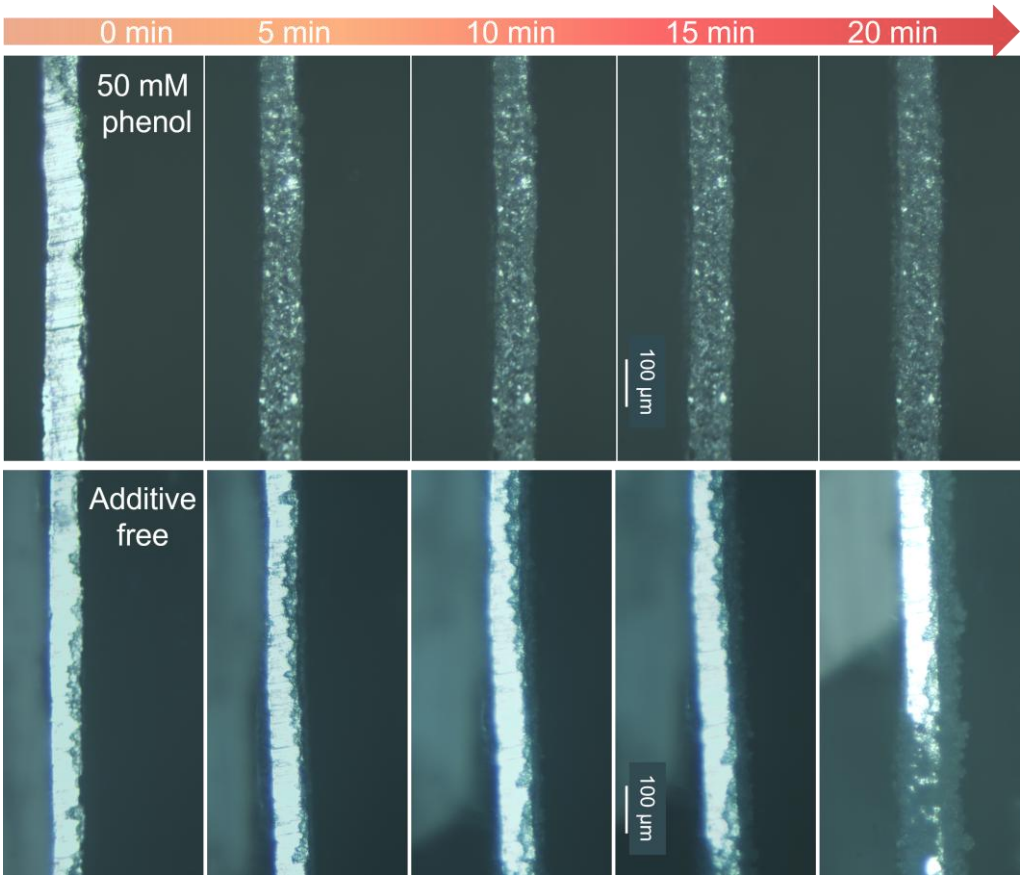

Figure S17. *In situ* optical microscopy investigation of Zn deposition in a home-made Zn/Zn cell with 50 mM phenol and additive-free electrolytes.

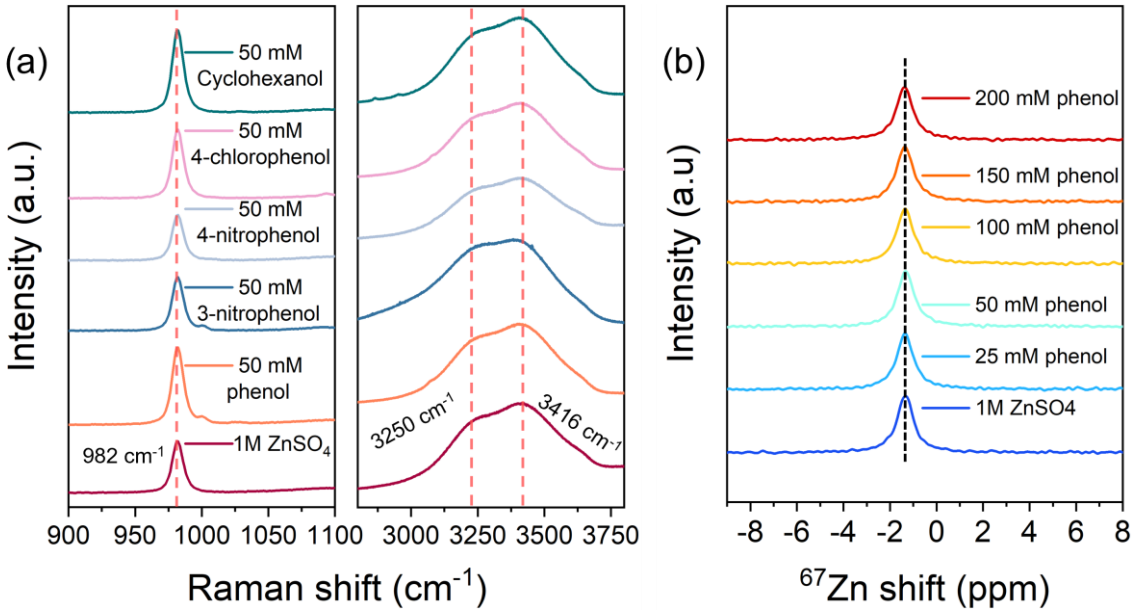

Figure S18. Solvation structure analysis by (a) Raman spectroscopy for different electrolytes and (b) NMR spectra of ^{67}Zn in different concentrations of phenol.

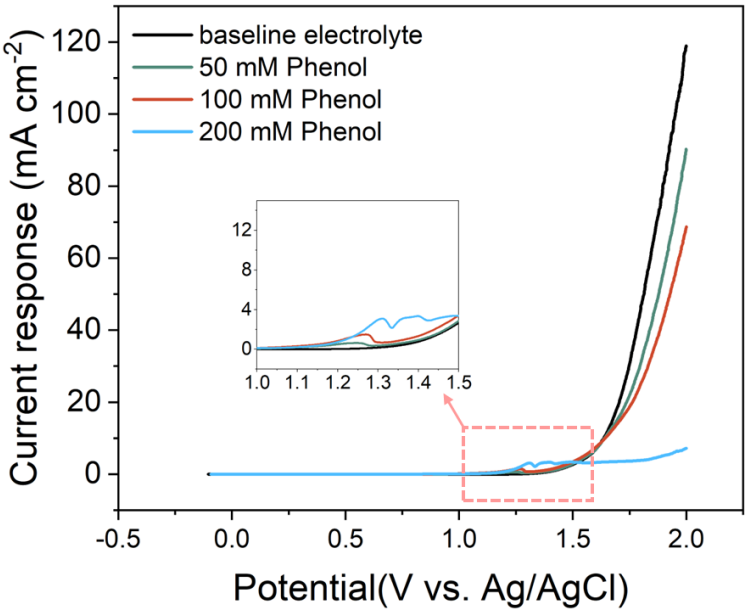

Figure S19. The oxidative stability of phenol, measured by LSV at 1 mV s^{-1} in Ti (WE)-Pt (CE)- Ag/AgCl (RE) configuration. All the electrolytes with different concentrations of phenol (50 mM, 100 mM, and 200 mM) exhibit a unique oxidation peak at 1.2-1.4 V vs. Ag/AgCl before the oxygen evolution reaction (OER), and the corresponding current response gradually increases with increasing phenol concentration. Hence, this peak can be ascribed to phenol

oxidation, which corresponds to 2.16-2.36 V vs. Zn^{2+}/Zn, highlighting the stability of phenol within the operating voltage window.

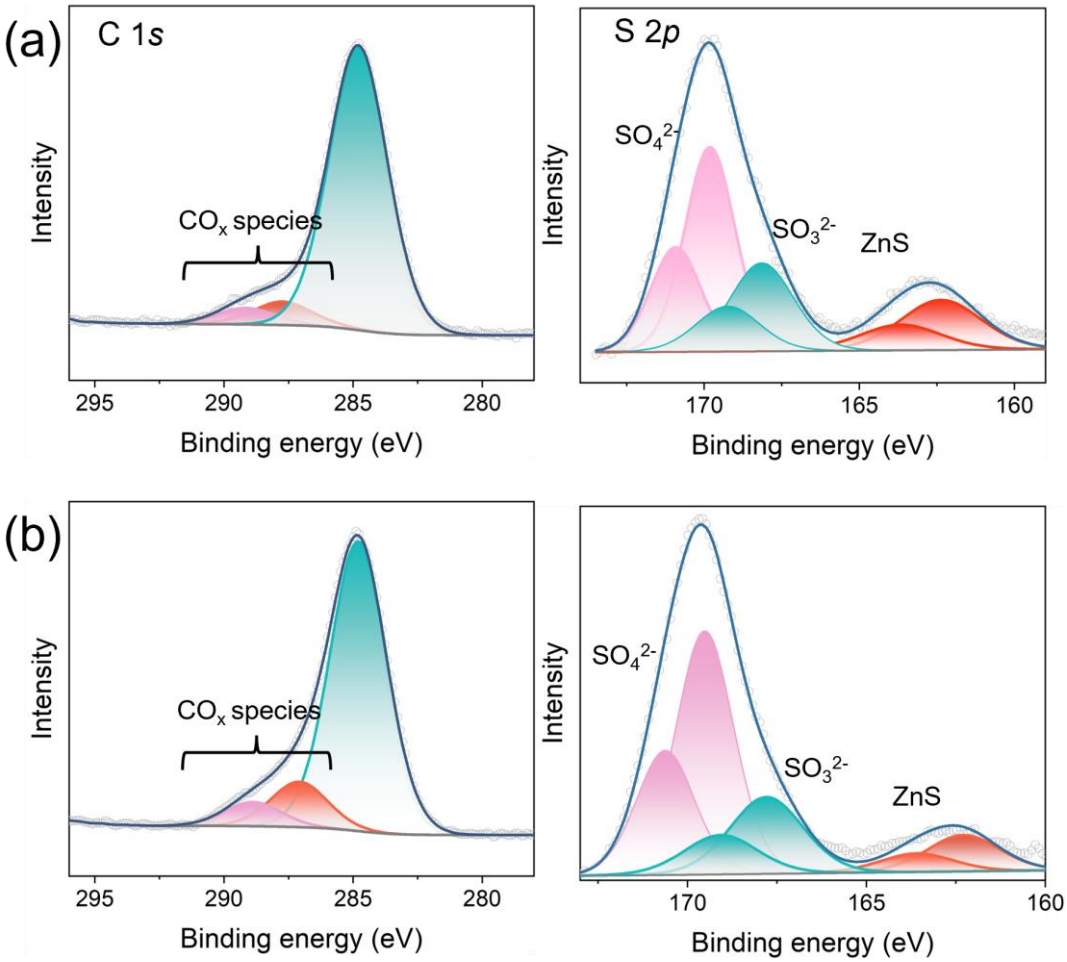

Figure S20. The surface C 1s and S 2p XPS spectra for the Zn electrode after 10 cycles in (a) 50 mM phenol and (b) additive-free electrolyte.

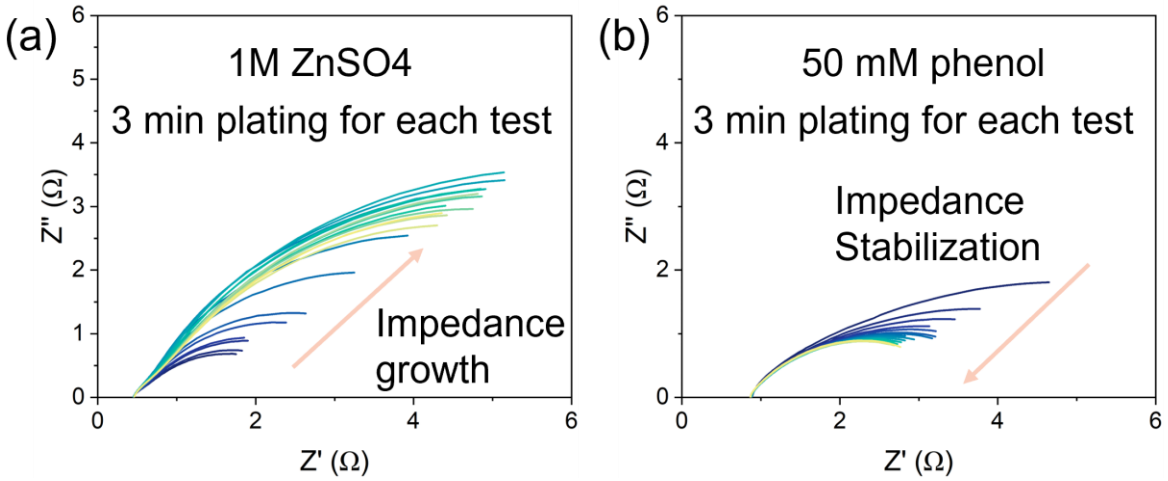

Figure S21. In situ EIS measurements obtained from Zn-Zn-Zn three-electrode configuration during initial deposition in (a) additive-free and (b) 50 mM phenol electrolytes for DRT analysis.

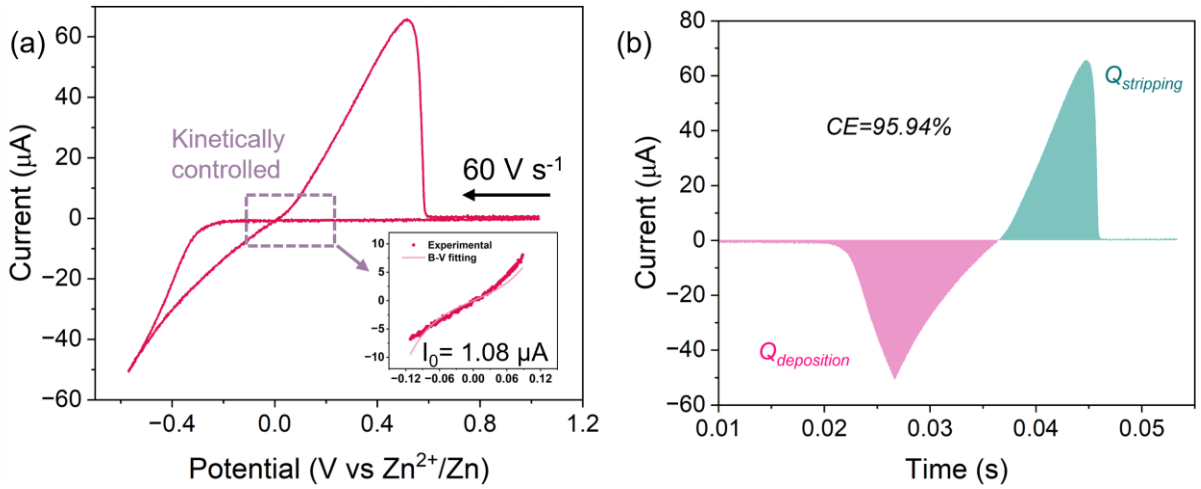

Figure S22. (a) Fast-scan cyclic voltammogram (60 V s^{-1}) recorded in 1M $ZnSO_4$ using a UME-Ag/AgCl two-electrode configuration. (b) Corresponding CE of Zn deposition/stripping in this electrolyte, derived from the cyclic voltammogram.

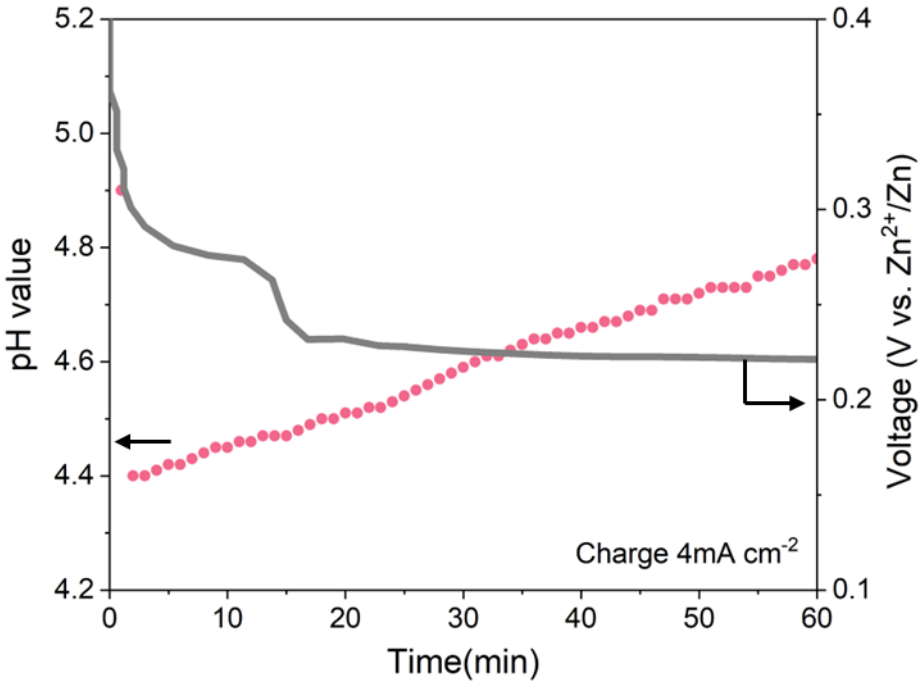

Figure S23. In situ pH measurements for additive-free electrolytes, measured at 4 mA cm^{-2}.

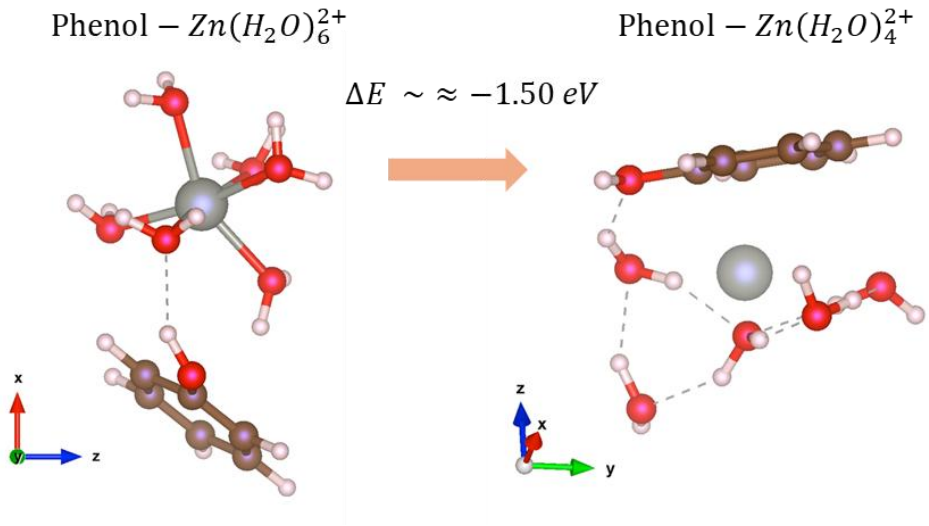

Figure S24. The internal energy (ΔE) difference between the initial state of phenol-$Zn(H_2O)_6^{2+}$and partially de-solvated state of phenol-$Zn(H_2O)_4^{2+}$after displacement of water molecules by phenol. The relative thermodynamic stability of these two solvation environments was quantified by calculating the change in internal energy (ΔE) for the substitution reaction. The native value of ΔE (~ -1.50 eV) confirms that the formation of the phenol-$Zn(H_2O)_4^{2+}$ is thermodynamically spontaneous and highly favorable

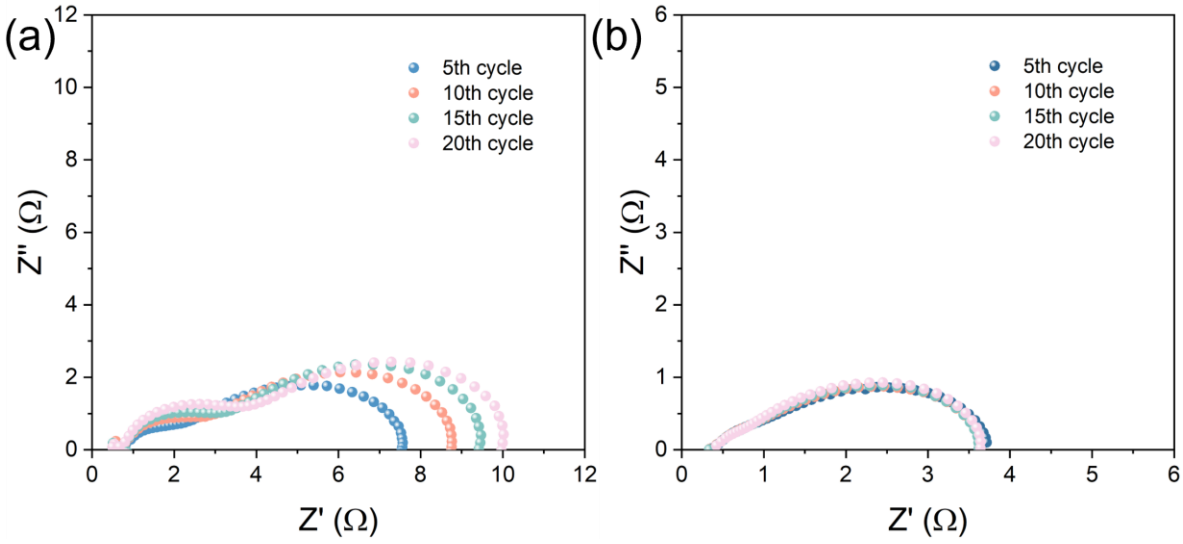

Figure S25. In situ EIS measurements obtained from Zn-Zn-Zn three-electrode configuration from 5 to 20 cycles in (a) additive-free and (b) 50 mM phenol electrolytes for DRT analysis.

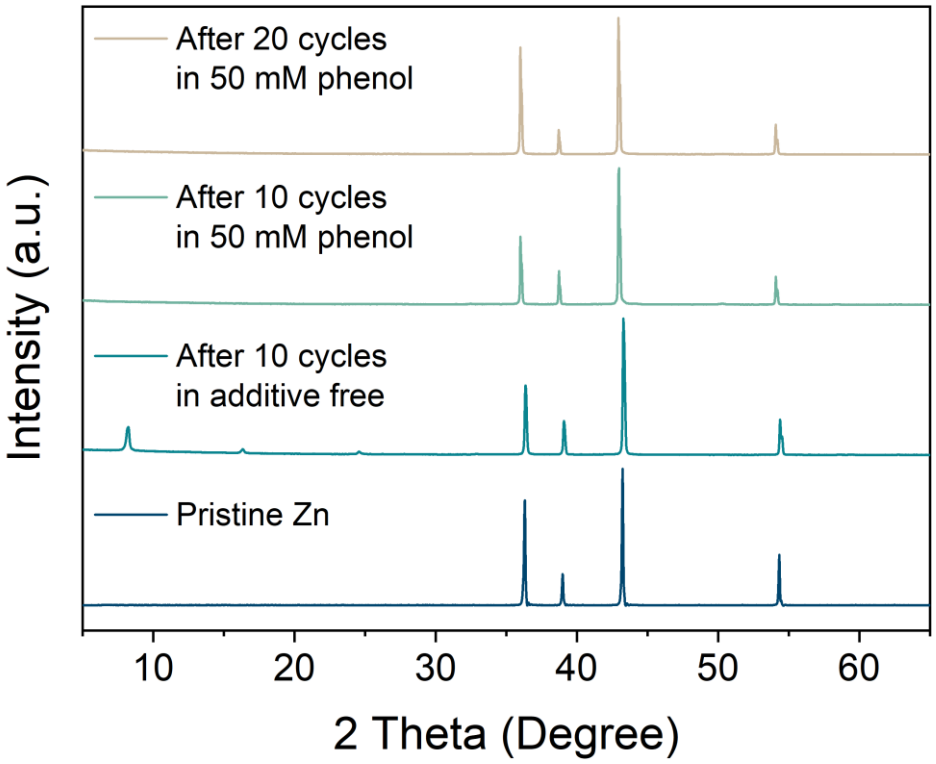

Figure S26. The XRD pattern for the plated Zn electrode after cycling in the two electrolytes.

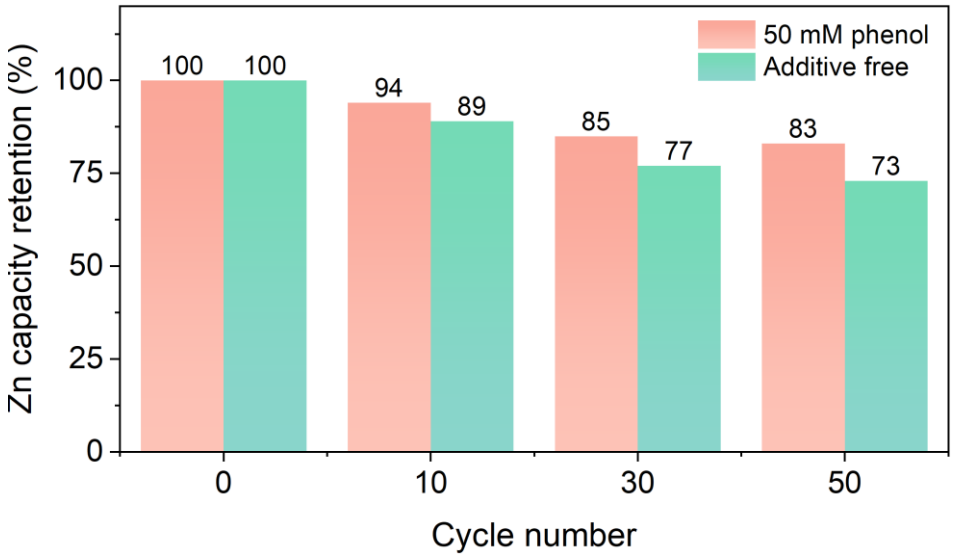

Figure S27.The remaining zinc capacity as a function of cycling in the two electrolytes.

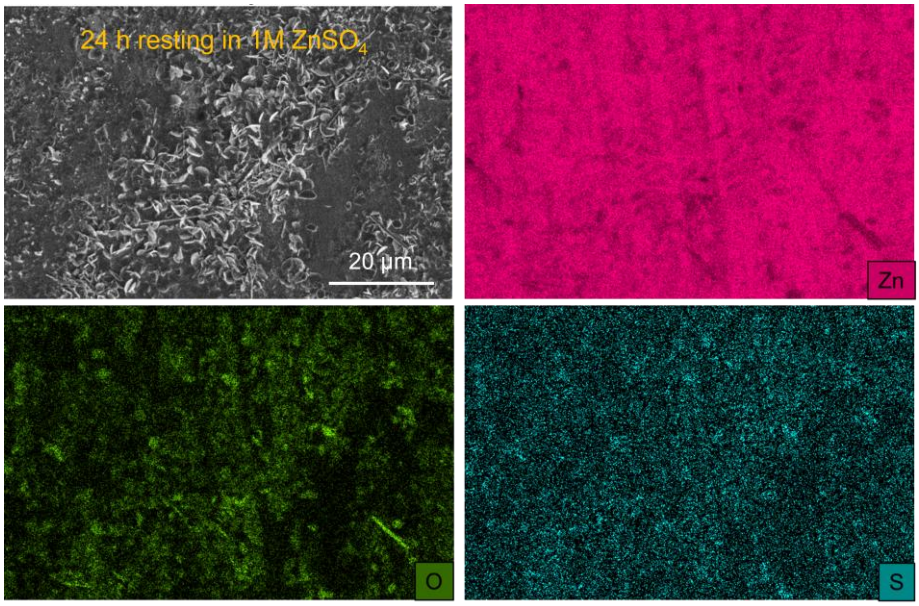

Figure S28. Representative SEM and EDS mapping images of Zn foil after 24 h soaking in the additive-free electrolyte.

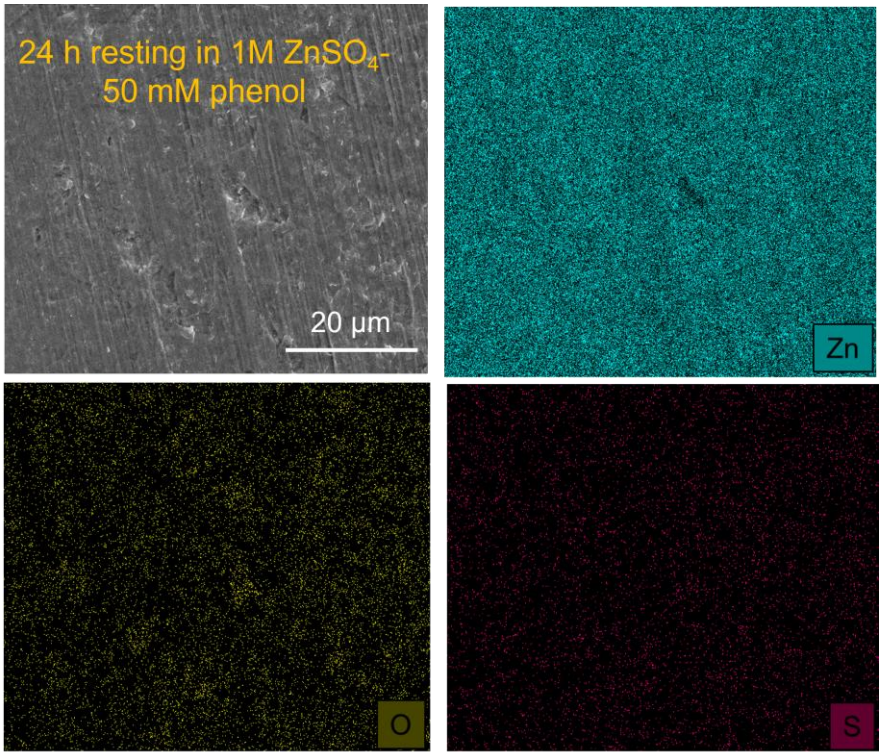

Figure S29. Representative SEM and EDS mapping images of Zn foil after 24 h soaking in the phenol-containing electrolyte.

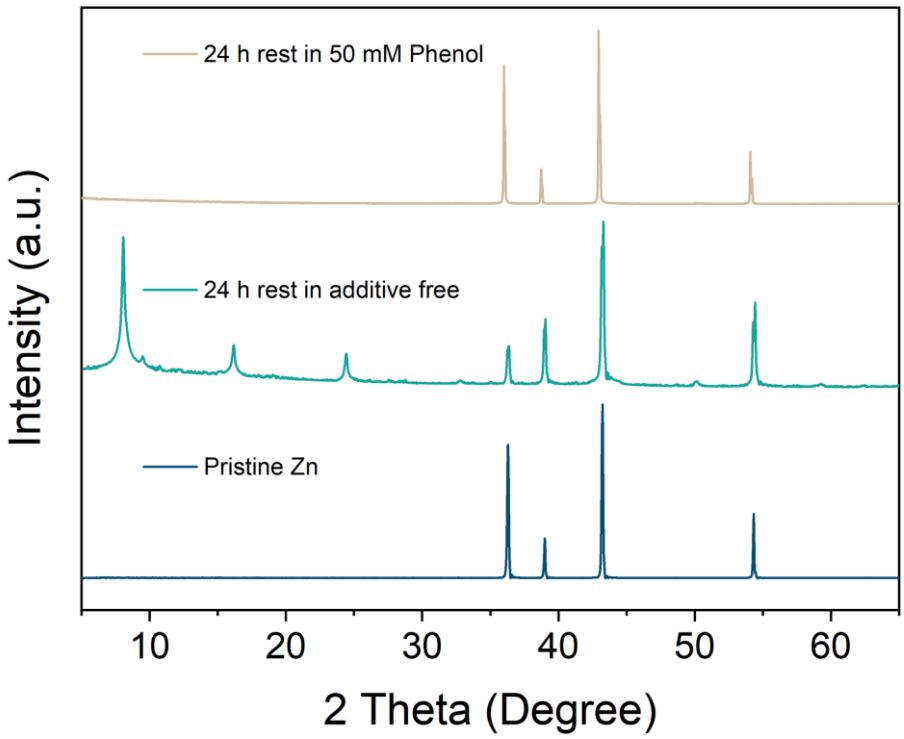

Figure S30. The XRD pattern for the Zn electrode after 24 h soaking in the two electrolytes.

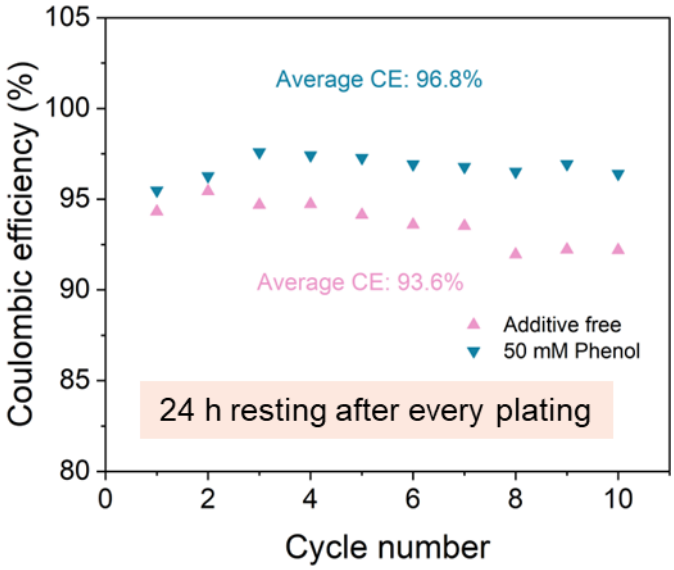

Figure S31. The CE evolution in Zn-Ti cells in the 50 mM phenol and additive free electrolyte with a 24-hour resting period between plating and stripping

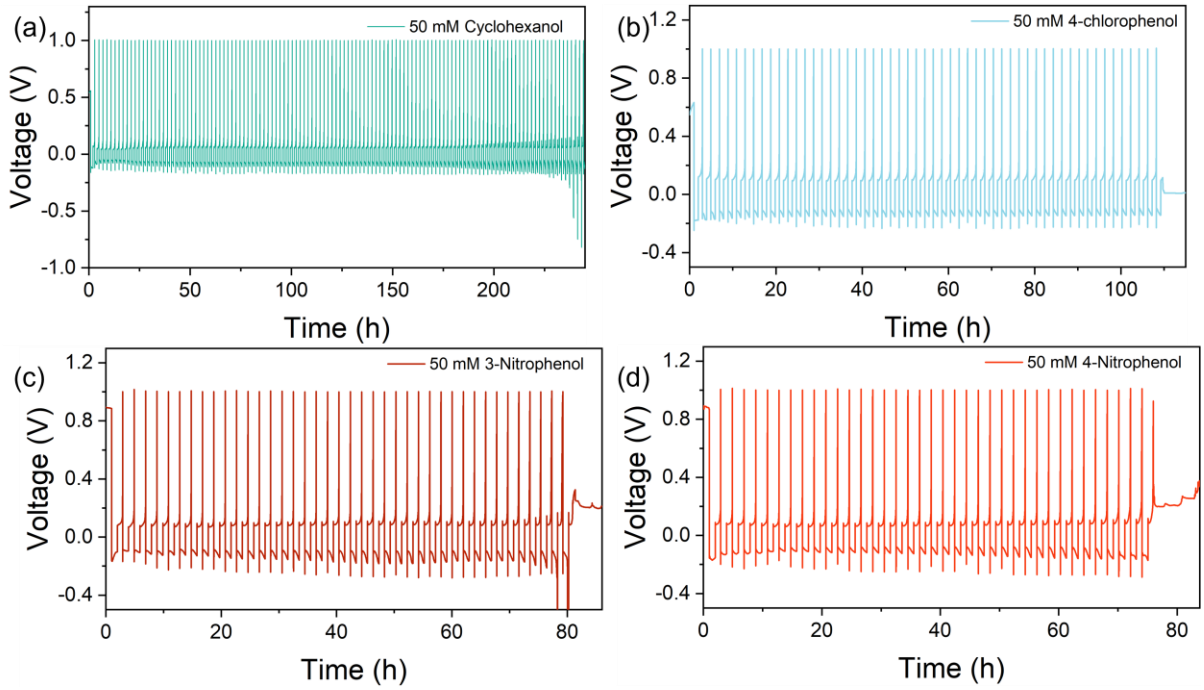

Figure S32. The galvanostatic zinc cycling in Zn||Ti configuration with (a) 50 mM cyclohexanol, (b) 50 mM 4-chlorophenol, (c) 50 mM 3-nitrophenol and (d) 50 mM 4-nitrophenol in the 1M $ZnSO_4$ electrolyte at 2 mA cm^{-2} and 2 mAh cm^{-2}.

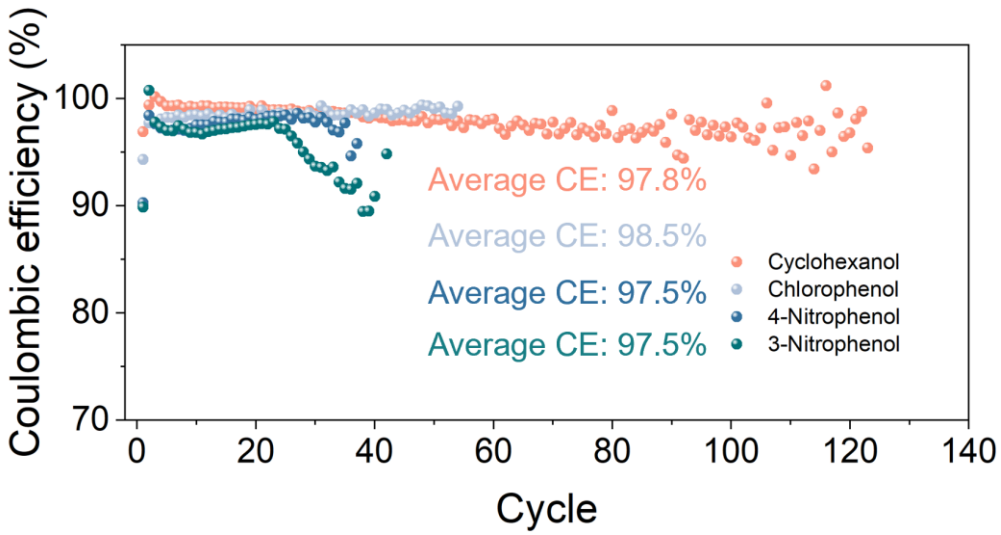

Figure S33. The corresponding Coulombic efficiency for cells cycled at 2 mA cm^{-2}-2 mAh cm^{-2} with different additives in the electrolyte.

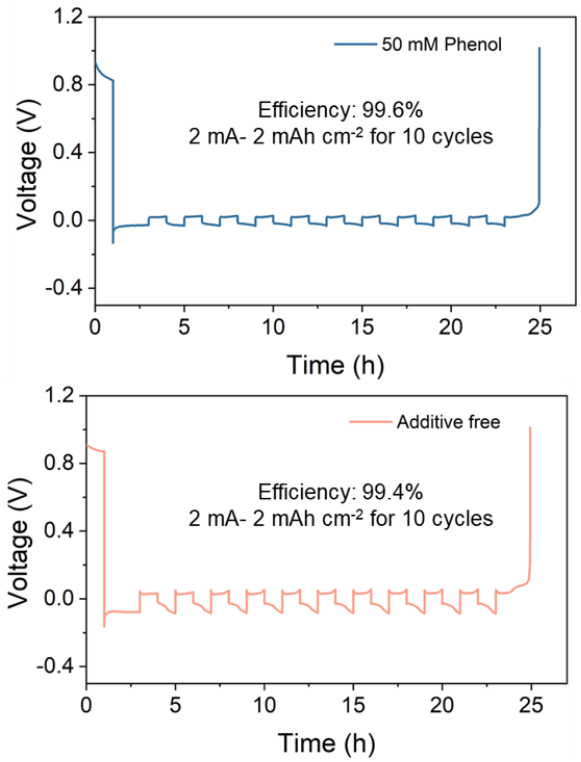

Figure S34. The polarization profile for the Aurbach method zinc cycling Coulombic efficiency measurement with the (a) 50 mM phenol and (b) additive-free electrolyte.

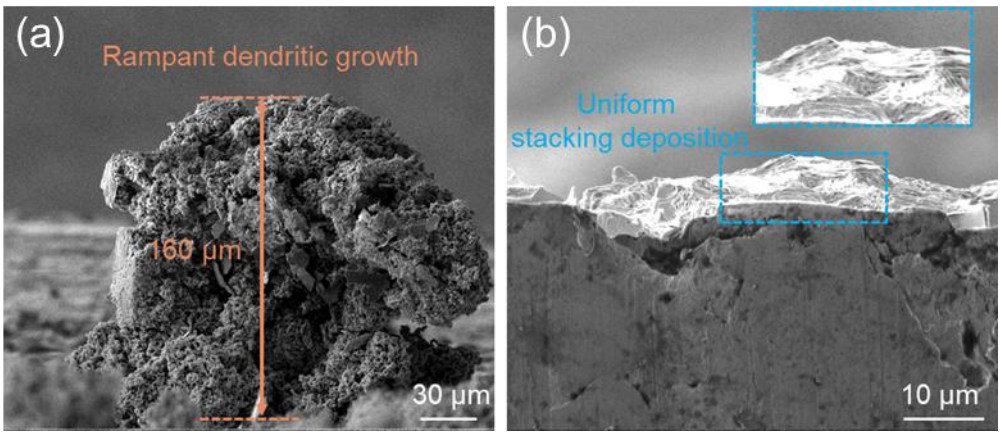

Figure S35. The cross-section SEM image of the Zn electrode after 10th plating at 2 mA-2mAh cm^{-2} in (a) the baseline and (b) 50 mM phenol electrolytes.

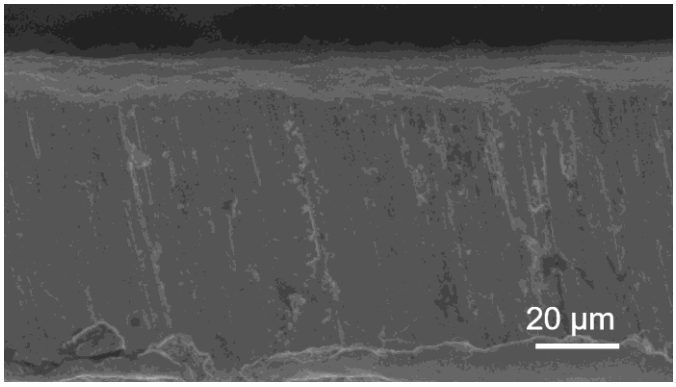

Figure S36. The cross-sectional SEM image for pristine Zn foil.

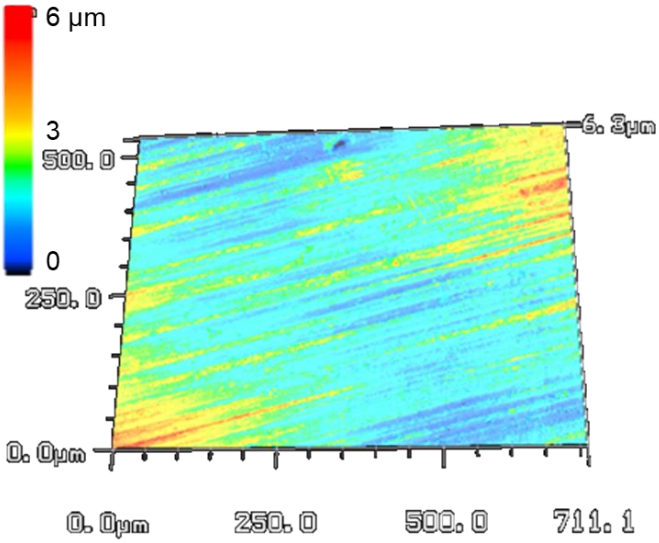

Figure S37. The LCSM image for pristine Zn foil.

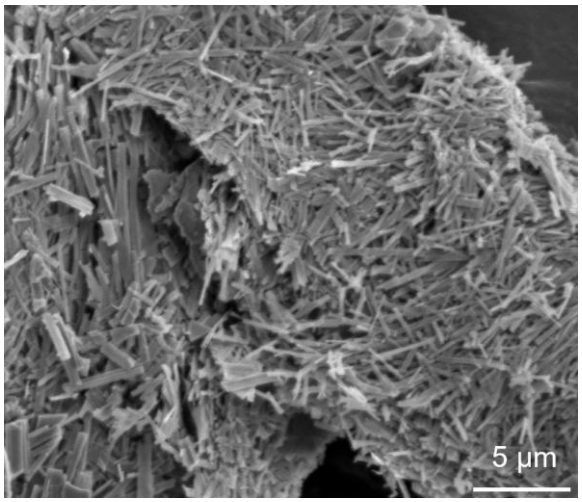

Figure S38. The nano-fiber morphology of as-prepared ZVO.

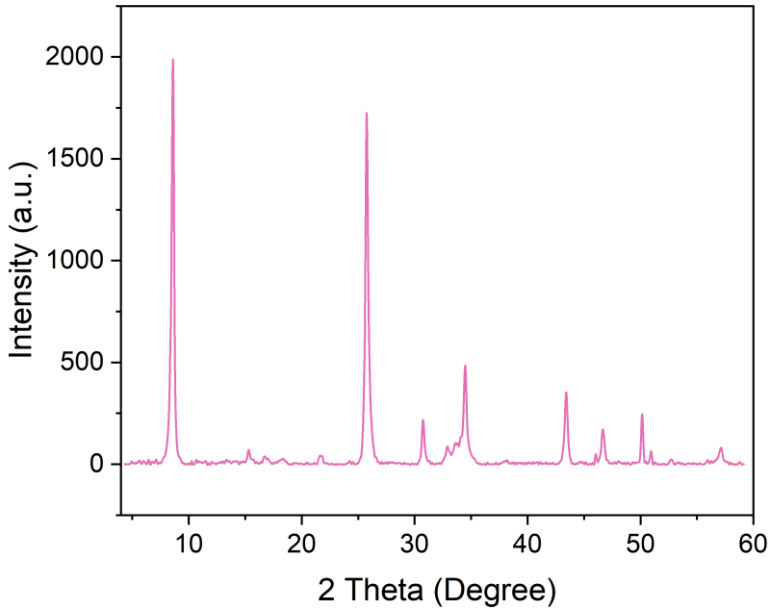

Figure S39. The XRD pattern of as-prepared ZVO.

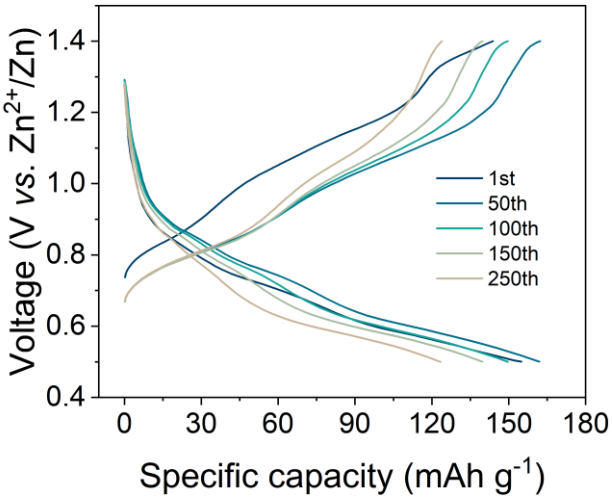

Figure S40. The voltage-capacity profiles for the ZVO||Zn cell cycling with the 50 mM phenol electrolyte at a current of 0.5 A g^{-1}.

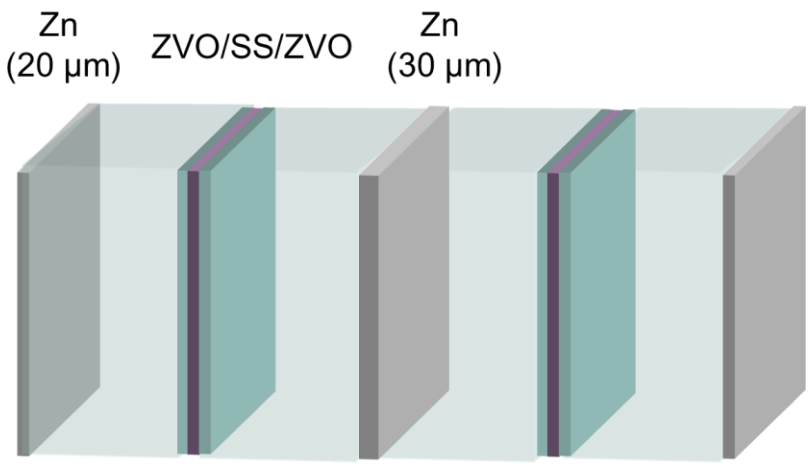

Figure S41. The scheme of the two-layer ZVO||Zn pouch cell with double-coated ZVO on stainless steel current collector.

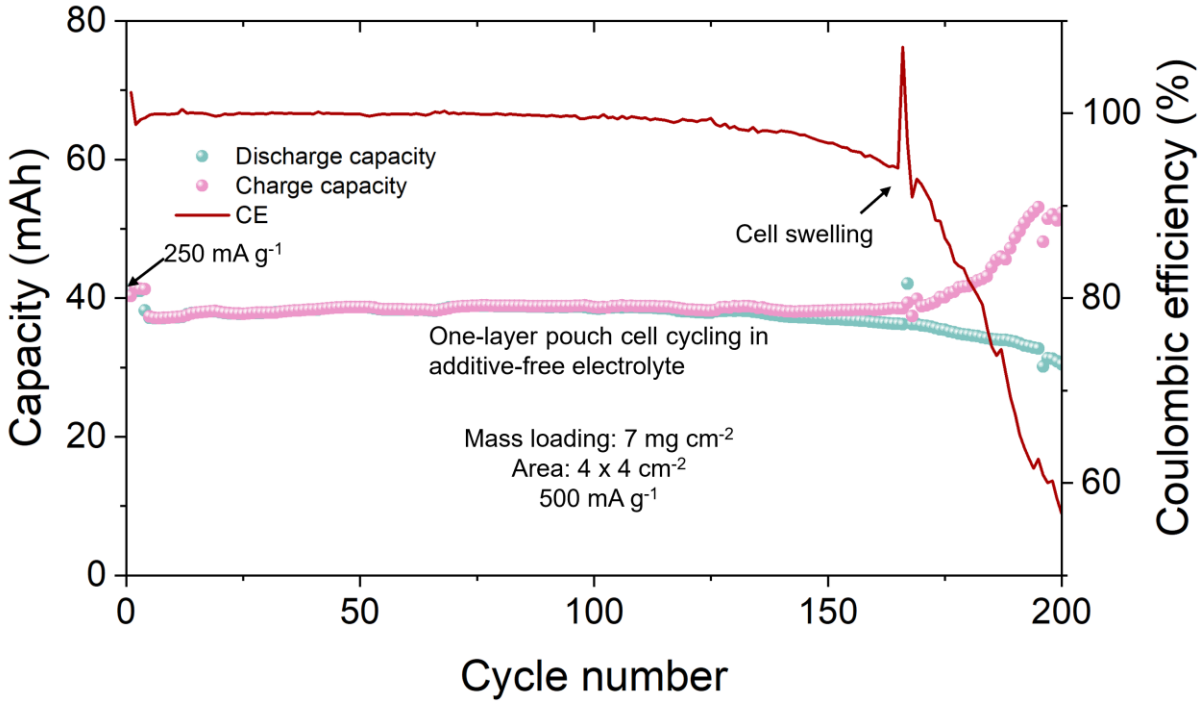

Figure S42. The corresponding cycling performance of ZVO||Zn pouch cell (4 cm × 4 cm, single layer cell with double-coated ZVO electrode) with 185 mg total ZVO loading, cycling in additive-free electrolyte at 0.5 A g^{-1}.